



TECHNISCHE
UNIVERSITÄT
WIEN
Vienna University of Technology

INSTITUT FÜR
MECHANIK UND
MECHATRONIK
Mechanics & Mechatronics



DISSERTATION

Railway catenary emulation on a Power-HiL test rig using model predictive impedance control

carried out for the purpose of obtaining the degree
Doctor technicae (Dr. techn.)
under the supervision of

Univ.Prof. Dipl.-Ing. Dr.techn. Stefan Jakubek

at the Institute of Mechanics and Mechatronics
Division of Control and Process Automation

submitted at TU Wien, Faculty of Mechanical and Industrial Engineering

by

Dipl.-Ing. Guilherme Aschauer
Mat.Nr.: 0627911



Vienna, March 16, 2022

Reviewed by

Alexander Schirrer
Institute of Mechanics and Mechatronics
TU Wien

João Pombo
Institute of Railway Research
University of Huddersfield, UK



Die approbierte gedruckte Originalversion dieser Dissertation ist an der TU Wien Bibliothek verfügbar.
The approved original version of this doctoral thesis is available in print at TU Wien Bibliothek.

This work was supported by the Austrian Research Promotion Agency (FFG) within the framework of the project Test Bed Control 841331.

I confirm, that going to press of this thesis needs the confirmation of the examination committee.

Affidavit

I declare in lieu of oath, that I wrote this thesis and performed the associated research myself, using only literature cited in this volume. If text passages from sources are used literally, they are marked as such.

I confirm that this work is original and has not been submitted elsewhere for any examination, nor is it currently under consideration for a thesis elsewhere.

I acknowledge that the submitted work will be checked electronically-technically using suitable and state-of-the-art means (plagiarism detection software). On the one hand, this ensures that the submitted work was prepared according to the high-quality standards within the applicable rules to ensure good scientific practice "Code of Conduct" at the TU Wien. On the other hand, a comparison with other student theses avoids violations of my personal copyright.

Vienna, March 16, 2022

Guilherme Aschauer



Die approbierte gedruckte Originalversion dieser Dissertation ist an der TU Wien Bibliothek verfügbar.
The approved original version of this doctoral thesis is available in print at TU Wien Bibliothek.

Acknowledgements

I would like to express my sincerest gratitude to my supervisor Stefan Jakubek for his invaluable assistance, scientific guidance throughout the project and his insightful comments and suggestions.

Furthermore, I would like to express my deepest thanks to Alexander Schirrer for his dedication and his support during (and after) my stay at the institute.

I also wish to thank Martin Kozek for his assistance and I am very grateful to all three of them for their encouragement and motivational guidance.



Die approbierte gedruckte Originalversion dieser Dissertation ist an der TU Wien Bibliothek verfügbar.
The approved original version of this doctoral thesis is available in print at TU Wien Bibliothek.

Kurzfassung

Die vorliegende Arbeit fasst die im Rahmen des Dissertationsprojekts “Test Bed Control” erarbeitenden Ergebnisse zusammen. Das Projekt wurde von der Österreichischen Forschungsförderungsgesellschaft (FFG, Projektnummer 841331) gefördert und war ein Kooperationsprojekt zwischen der Fa. MELECS (bzw. in weiterer Folge Siemens) und dem Institut für Mechanik und Mechatronik (Abteilung für Regelungstechnik und Prozessautomatisierung) der Technischen Universität Wien.

Projektziel war die Echtzeitemulation der verteilt-parametrischen Oberleitungsdynamik auf einem Power-Hardware-in-the-Loop (PHiL) Pantographenprüfstand um realitätsnahe Tests von Hochgeschwindigkeitsstromabnehmern bereits vorab im Labor durchführen zu können und so Einsparungen bei kostspieligen und aufwendigen Zulassungsfahrten zu erzielen.

Harte Echtzeitanforderungen sowohl an die Simulation des zugrundeliegenden mathematischen Oberleitungsmodells als auch an die Prüfstandsregelung müssen erfüllt werden. Dies geht jedoch idealerweise nicht zulasten der Modellgüte und so werden hier wesentliche Resultate des Modellierungsprozesses dargestellt. Dies betrifft unter anderem die Herleitung von absorbierenden Randbedingungen für die Finite-Elemente und Finite-Differenzen diskretisierten partiellen Differentialgleichungen (Euler-Bernoulli-Balken unter axialer Vorspannung) als auch das anschließend eingesetzte, optimierte Integrationsverfahren.

Ein modellprädiktiver Impedanzregler wird entwickelt, der die Dynamik des nichtlinearen, echtzeitfähigen Oberleitungsmodells am Stromabnehmerprüfstand einregelt und erlaubt so die komplexe Interaktion Stromabnehmer/Oberleitung bereits vorab im Labor zu untersuchen.

Die Konsistenz in den physikalischen Erhaltungsgrößen Impuls und Energie, die permanent zwischen Stromabnehmer und Prüfstand bzw. zwischen Stromabnehmer und Oberleitungsmodell ausgetauscht werden, wird durch eine eigens eingeführte virtuelle Korrekturkraft sichergestellt. Dies führt zu einer realitätsnahen Kopplung zwischen Prüfling und Prüfstand.

Im ersten Teil der Arbeit wird eine kurze Einführung in die Problemstellung und Motivation gegeben. Im Anschluss werden die Projektziele dargestellt und die entwickelte Methodik zur Erreichung derselbigen skizziert. Nach einer Übersicht der wissenschaftlichen Erkenntnisse folgt abschließend ein Abdruck der veröffentlichten Beiträge in Peer-Review-Zeitschriften.



Die approbierte gedruckte Originalversion dieser Dissertation ist an der TU Wien Bibliothek verfügbar.
The approved original version of this doctoral thesis is available in print at TU Wien Bibliothek.

Abstract

This thesis summarizes the main (academic) results developed by the applicant during the three year period of the project “Test Bed Control”, an FFG-funded (Austrian Research Promotion Agency, project number 841331) cooperation between MELECS (respectively Siemens) and the Institute of Mechanics and Mechatronics, Department of Process Automation and Control at the Vienna University of Technology.

The project’s goal was to emulate the distributed-parameter dynamics of a railway catenary on a full-scale pantograph power hardware-in-the-loop (PHiL) test rig to allow for close-to-reality testing of trains’ current collectors (also called pantographs).

Strict real-time requirements on the mathematical model and the test rig control tasks had to be met. Key results of the modeling process to derive at a nonlinear real-time-capable catenary model that still retains high-fidelity are presented. Therefore, absorbing boundaries for the finite-difference and finite-element discretized (moving) Euler-Bernoulli-Beam (EBB) dynamics were constructed.

A model predictive impedance controller is then deployed on a full-scale pantograph test rig to emulate the nonlinear catenary dynamics to the unit under test (UUT). The consistency in the conserved quantities momentum and energy that are permanently exchanged between the unit-under-test and the test rig respectively the catenary model have been guaranteed by an artificial virtual correction force to allow for a physically accurate coupling between the test rig and the pantograph.

In the first part of the current work a short summary including the problem statement and motivation is given. Then the goals of the project are formulated and afterwards the methodology developed and applied to reach these goals is sketched. The summary of the scientific results is followed by the scientific contributions of the applicant’s dissertation. The second part contains reprints of peer-reviewed journal publications.



Die approbierte gedruckte Originalversion dieser Dissertation ist an der TU Wien Bibliothek verfügbar.
The approved original version of this doctoral thesis is available in print at TU Wien Bibliothek.

Contents

I	Introduction	1
1	Motivation	2
2	Goals	4
3	Methodology	5
3.1	Catenary modeling	6
3.1.1	Moving Coordinate Transformation	7
3.1.2	Discretization of PDEs	7
3.1.2.1	Finite-Difference Method	7
3.1.2.2	Finite-Element Method	8
3.1.3	Newmark Time-Integration	11
3.1.4	Absorbing Boundaries for Partial Differential Equations	12
3.1.5	Optimization-Based Approach	13
3.1.5.1	Performance Criterion	13
3.1.5.2	Stability Criterion	14
3.1.5.3	Results	14
3.1.6	Control-Based Approach	14
3.1.6.1	Extension of the Computational Domain	16
3.1.6.2	Modal Approximation of the Wave Field	17
3.1.6.3	Construction of the Reference Solution	17
3.1.6.4	Formulation of the Control Problem	18
3.1.6.5	Results	18
3.1.7	Summary of Catenary Modeling	18
3.1.8	Results	20
3.1.9	Simplified Catenary Model for Linear Control Design	20
3.2	Test Rig Impedance Control	23
3.2.1	Test Rig Control	23
3.2.2	Conserved Quantities	24
3.2.3	Impedance Control	26
3.3	Results of the Test Rig Catenary Emulation	29
3.3.1	Implementation Details	29
3.3.2	Results	30

4 Summary of the scientific publications	32
5 Scientific contributions of the applicant	33
Bibliography	35
II Publications – Main Body of the Thesis	41
5.1 Publication A	42
5.2 Publication B	43
5.3 Publication C	44
5.4 Publication D	45

Part I

Introduction

Chapter 1

Motivation

The requirements for modern (high-speed) pantographs are strongly increasing. They have to establish a stable connection with the catenary under all operating conditions, including different train configurations and weather conditions. Additionally, strict requirements on the resulting contact force are imposed by norms and national regulations. Not only is a corridor for the velocity-dependent mean contact force defined in EN 50367 but more recent issues of this standard for example also regulate the contact force's variance. This leads to increased efforts and costs in the homologation process, where cumbersome track tests are necessary to tune the pantograph's airfoils and static contact force. This is especially true for multi-traction operation, where more than one pantograph is in contact with the catenary, and all of them need to meet the norm requirements.

One promising approach to reduce homologation risks and the amount of (unplanned) track tests are power hardware-in-the-loop (PHiL) tests, where the pantograph is put in interaction with a virtual catenary on a test rig. The test rig should then behave like a real-world catenary and so the dynamics of the catenary/pantograph interaction could already be investigated and tuned beforehand in the laboratory.

However, significant challenges have to be mastered before reaching the goal of realistically emulating the catenary behavior on a test rig. The catenary dynamics show complex distributed-parameters wave propagation phenomena and nonlinearities due to one-sided droppers (attached to the carrier wire and effectively holding the contact wire). At these droppers, partial wave reflections occur and they additionally show very low stiffness when compressed. Lastly, one continuous segment of the catenary is often way longer than 1 km which could easily render the resulting computational domain too large for real-time computations, as necessary for PHiL tasks. Artificially reducing the computational domain leads to spurious reflections of the just weakly-damped oscillations on the newly introduced computational boundaries which drastically reduces the catenary model's fidelity. One approach to face this problem are absorbing boundaries that, however, have so far not been derived for the (moving) Euler-Bernoulli beam under axial pre-tension.

Even with a real-time capable catenary model at hand, the task of tracking its dynamics on a test rig is challenging. Suitable impedance control concepts need to be developed that take the special catenary model structure into account and control the test rig actuators to follow the catenary's dynamics.

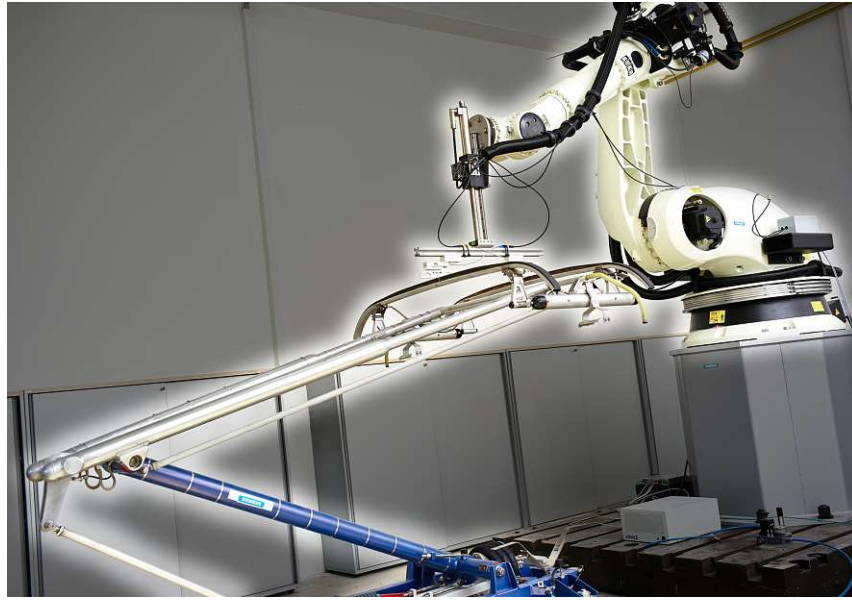


Figure 1.1 Full-scale PHiL pantograph test rig of Siemens Mobility Austria GmbH

Finally, an accurate PHiL test run not only tracks the relevant dynamics but also establishes a reliable, stable, and physical-trustworthy coupling between the UUT and the test rig, respectively the virtual catenary by tracking the exchanged conserved quantities momentum and energy at both interfaces. Because of test rig limitations (limited-bandwidth actuation, modeling errors, ...), a drift in the energy error may occur and special care has to be taken to obtain trustworthy PHiL test runs.

Chapter 2

Goals

In order to reach the final objective of a high-fidelity catenary emulation on a PHiL test rig the following tasks have to be mastered:

1. development of a high-fidelity real-time capable catenary model,
2. design of an impedance controller that emulates the model's dynamics on the test rig,
3. implementation of the catenary emulation on a full-scale pantograph test rig,
4. ensure physical trustworthy PHiL test runs by proper impedance coupling between the test rig and the UUT.

Different model reduction techniques were implemented and evaluated to finally obtain a satisfactory catenary model. First, the catenary is mathematically white-box modeled, resulting in two PDEs that are coupled via nonlinear (one-sided) stiffnesses. Then, a coordinate transformation is applied to obtain a pantograph-fixed formulation of the catenary dynamics, which now moves through the computational domain. Two general, widely-applicable methods to construct absorbing boundary layers were formulated to allow for shorter computational domains without the negative side effects of wave reflection at the artificial domain boundaries.

To reach the second goal, a model predictive impedance controller was developed that incorporates a test rig model as well as a reduced version of the nonlinear real-time catenary model. The control goal is to drive the position and velocity differences between both models to zero by using the test rig actuation. Due to the predictive nature of the controller the phase-lag is almost completely eliminated and constraints on the test rig actuation are incorporated in the control design too.

However, tracking just position and velocity is not sufficient as this may result in a drift in the exchanged energy. Thus, the energy transfer between (1) the UUT and the test rig and (2) the UUT and the catenary model are tracked. A virtual correction force as an additional control input of the MPC is introduced. This force acts in addition to the measured contact force as an input to the catenary model and is utilized to reduce the momentum and energy error during the test run.

Chapter 3

Methodology

In this section, the main methods that were developed and applied to reach the goals formulated in Chapter 2 are briefly outlined, and references to the author's own publications and further literature are provided.

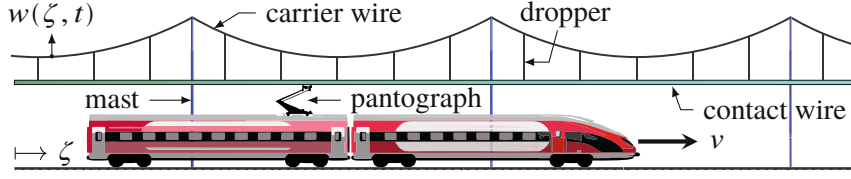


Figure 3.1 Typical catenary set-up with a train moving with velocity v .

3.1 Catenary modeling

Figure 3.1 shows a typical catenary with its main components. Via droppers the contact wire is attached to the carrier wire which itself is mounted on masts. The droppers show very high stiffness when elongated and negligible resistance when subjected to pressure. Usually, their lengths are adjusted in a way that warrants uniform stiffness in vertical direction. The carrier, as well as the contact wire, can both be well described by Euler-Bernoulli bending beams (EBB) under axial pretension [1, 2]:

$$\rho A w_{tt} + \beta w_t + EI w_{\zeta\zeta\zeta\zeta} - T w_{\zeta\zeta} = f(\zeta, t), \quad (3.1)$$

with the displacement field $w(t, \zeta)$ over time t and spatial coordinate ζ and a subscript denotes derivatives w.r.t. to the coordinate. ρA is the mass per unit length, β a coefficient of velocity-proportional damping, EI the bending stiffness, and T is the axial tensile force.

The masts can either be modeled via fixed carrier wire segments or via very stiff springs (as done here via a force density):

$$f_{m,i,ca}(\zeta, t) = -\delta(\zeta - \zeta_{m,i}) k_m w_{ca}(\zeta_{m,i}, t), \quad (3.2)$$

with the Dirac delta distribution δ , $\zeta_{m,i}$ as the position of mast number i , and the displacement of the carrier wire at the mast's positions: $w_{ca}(\zeta_{m,i}, t)$.

The droppers are modeled as one-sided stiffnesses that are only active in tensile direction and act on the contact and carrier wires:

$$\begin{aligned} f_{d,i,co}(\zeta, t) &= -f_{d,i,ca}(\zeta, t) = \delta(\zeta - \zeta_{d,i}) F_{d,i}(t) \\ F_{d,i}(t) &= \begin{cases} k_{d,i} (l_{d,i}(t) - l_{d,i,0}) & \text{if } l_{d,i}(t) > l_{d,i,0} \\ 0 & \text{otherwise} \end{cases} \end{aligned} \quad (3.3)$$

with $l_{d,i,0}$ as the undeformed length of dropper i , its instantaneous length $l_{d,i}(t)$, and stiffness $k_{d,i}$.

The pantograph moves with constant velocity v along the catenary and generates a point force:

$$f_{panto,co}(\zeta, t) = \delta(\zeta + vt - \zeta_{panto,0}) F_{panto}(t), \quad (3.4)$$

with the pantograph's initial position $\zeta_{panto,0}$.

A realistic model of the catenary is formulated by Eqs. (3.1)–(3.4). Different solution techniques (e.g. Finite-Differences (FD) or Finite-Elements (FE)) exist to solve such a system of coupled PDEs.

However, one continuous section of contact wire is often 1500 m long and computing such a long segment with high-fidelity in real-time is not yet realizable with today's hardware.

3.1.1 Moving Coordinate Transformation

To describe the dynamics of Eq. (3.1) in moving coordinates a new spatial coordinate is introduced, as published in [3]:

$$x = \zeta - vt. \quad (3.5)$$

The equation of motion (3.1) for the displacement field $w = w(x, t)$ now reads:

$$\rho A w_{tt} + \beta w_t = -EI w_{xxxx} + (T - \rho A v^2) w_{xx} + \beta v w_x + 2v \rho A w_{tx} + f, \quad (3.6)$$

with the boundary conditions:

$$\begin{aligned} x \in \mathcal{D}, \quad \mathcal{D} = \left\{ x \mid -\frac{L_{\text{domain}}}{2} \leq x \leq \frac{L_{\text{domain}}}{2} \right\} \\ w(x \in \partial \mathcal{D}, t) = w'(x \in \partial \mathcal{D}, t) = 0, \quad t \geq 0, \end{aligned} \quad (3.7)$$

The spatial coordinate x now moves with train speed v and the pantograph is thus fixed in the computational domain, through which the whole catenary now travels. Figure 3.2 visualizes this situation. The computational domain is described by the red rectangle and the absorbing layers (derived in Section 3.1.6) are in the intervals $x \in [-\frac{L_{\text{domain}}}{2}, -\frac{L_{\text{interior}}}{2}]$ and $x \in [\frac{L_{\text{interior}}}{2}, \frac{L_{\text{domain}}}{2}]$. Additionally, the different wave speeds in up- and downstream direction (Doppler-effect) are sketched in the upper part of Figure 3.2.

3.1.2 Discretization of PDEs

Different methods exist for solving PDEs like (3.6)-(3.7), the most well-known being the Finite-Difference method (FDM), the Finite-Element method (FEM), or the Fourier-Galerkin method. For the former two absorbing boundaries for Eq. (3.6) were obtained using two different approaches. Both discretization methods will be briefly introduced.

3.1.2.1 Finite-Difference Method

The FDM divides the (spatial and temporal) solution space into a uniform grid and approximates the derivatives in the PDE by differential quotients, built by using the solution values at adjacent grid points.

May a function $u(x)$ be sufficiently smooth and differentiable, then a Taylor-series approximation can be formulated around an arbitrarily chosen point x_0 :

$$u(x_0 + h) = u(x_0) + hu'(x_0) + \mathcal{O}(h^2). \quad (3.8)$$

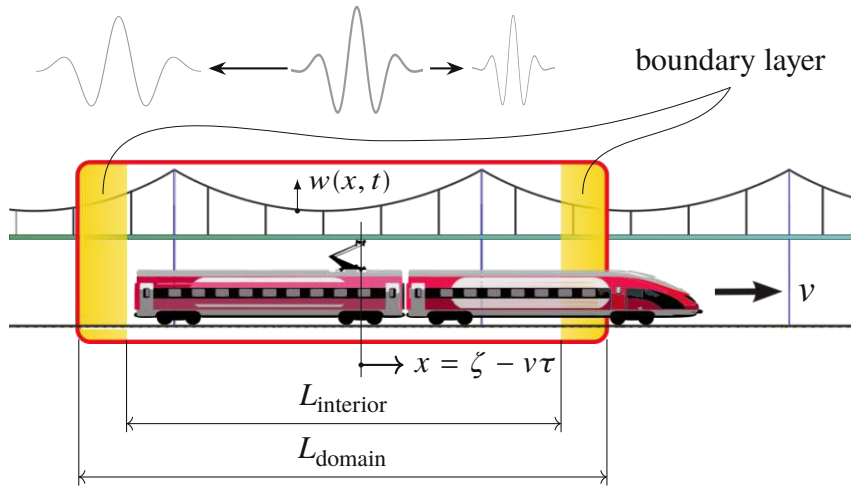


Figure 3.2 The catenary model from Figure 3.1 after applying the coordinate transformation (3.5). The pantograph now remains at a fixed position x_{panto} while the catenary moves through the computational domain. The absorbing boundary layers are shown in yellow, and at the top, the different wave propagation speeds in up- and downstream direction are sketched.

Eq. (3.8) is an approximation of the original function's value at $x_0 + h$ provided that h is sufficiently small. Rearranging leads to an approximation of the first derivative by using the function values $u(x_0)$ and $u(x_0 + h)$:

$$u'(x_0) \approx \frac{u(x_0 + h) - u(x_0)}{h}, \quad (3.9)$$

and is called forward Euler method. By utilizing higher-order terms or algebraic operations of Taylor-series', different (more sophisticated) approximations can be obtained.

For a one-dimensional problem like (3.6) with discretizations Δx and Δt the solution grid is shown in Figure 3.3. The geometric arrangement of nodal values that are needed for the computation of new values is called stencil. One is exemplarily shown in Figure 3.3 for the interior nodes of the EBB (in green). Additionally, since the green stencil can not be applied for the computation at nodes with $k = 0$ and $k = 1$, a generic boundary stencil is sketched (in blue).

3.1.2.2 Finite-Element Method

With the FEM the solution domain is split into small elements and the solution field on each element is approximated via simple trial-functions which have strong local support, i.e. are only active on the corresponding element (respectively its vicinity), such that the overall solution can be obtained by summation over all elements.

First, the original problem (3.6) is written in implicit form:

$$D(w(x, t)) = \rho A w_{tt} + \beta w_t + EI w_{xxxx} - (T - \rho A v^2) w_{xx} - \beta v w_x - 2v \rho A w_{tx} - f = 0, \quad (3.10)$$

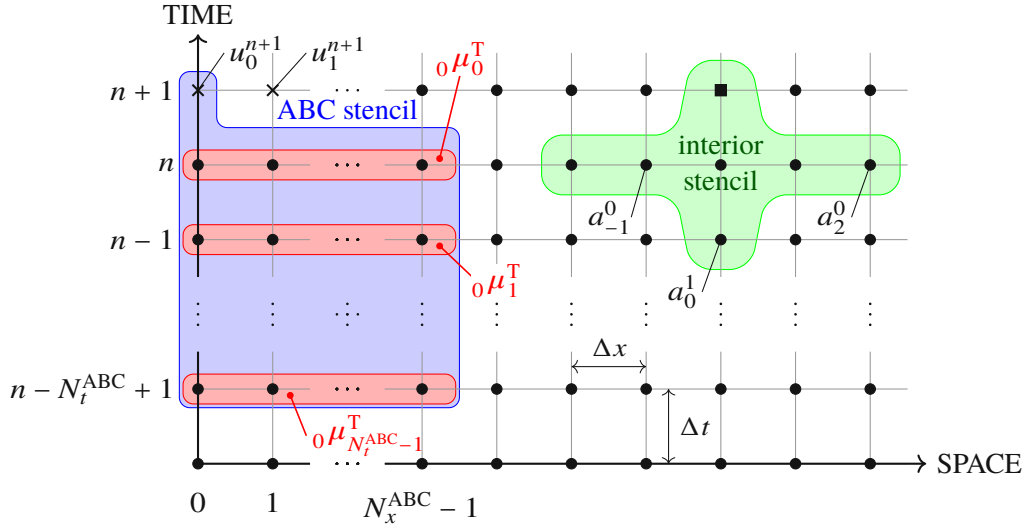


Figure 3.3 An explicit interior stencil (green) for the EBB and a generic boundary layer stencil for $k = 0$.

and multiplied with test functions $\psi_i : \mathcal{D} \rightarrow \mathbb{R}$ and integrated over the computational domain \mathcal{D} :

$$\int_{\mathcal{D}} \psi_i(x) D(w(x, t)) dx = 0, \quad \text{for } i = 1, \dots, 2n_e, \quad (3.11)$$

with $n_e - 1$ being the number of finite elements in the computational domain. The displacement field $w(x, t)$ is then approximated by a linear combination of $2n_e$ trial functions, that are chosen here to be identical to $\psi_i(x)$:

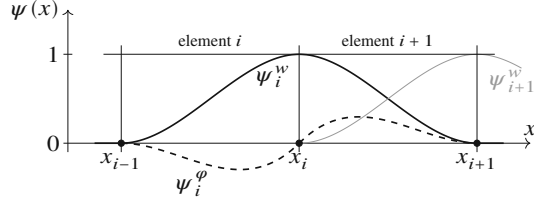
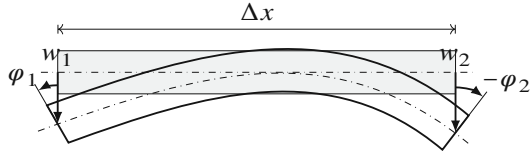
$$w(x, t) \approx \bar{w}(x, t) = \sum_{i=1}^{2n_e} \psi_i(x) q_i(t), \quad \text{with } q_i(t) : \mathbb{R} \rightarrow \mathbb{R}, \quad (3.12)$$

The node displacements w_i and rotations $\varphi_i = \frac{\partial w_i}{\partial x}$ of the nodes are chosen as time-dependent coefficients $q_i(t)$, see Figure 3.4a. The trial functions are accordingly split into $\psi_i^w(x)$ and $\psi_i^\varphi(x)$ and describe the contribution of the particular degree of freedom (DoF) to the overall solution. They are chosen to have only local support and are zero on almost the whole domain, see Figure 3.4b. Using (3.12) in the weak formulation (3.11) yields $2n_e$ ordinary differential equations for the $2n_e$ unknowns $q_i(t)$:

$$\int_{\mathcal{D}} \psi_i(x) D \left(\sum_{j=1}^{2n_e} \psi_j(x) q_j(t) \right) dx = 0, \quad \text{for } i = 1, \dots, 2n_e. \quad (3.13)$$

All DoFs are collected into one vector \mathcal{Q}_c (with subscript c as a placeholder for ca (carrier) or co (contact wire):

$$\mathcal{Q}_c(t) = [w_1(t) \quad \varphi_1(t) \quad \dots \quad w_{n_e}(t) \quad \varphi_{n_e}(t)]^T. \quad (3.14)$$



(a) Hermitian beam element of which the FEM-discretized EBB is made up. Each node has one displacement and one rotational DoF (w respectively φ). The undeformed beam element is sketched in gray.

(b) Shape functions $\psi_i^w(x)$ (solid) and $\psi_i^\varphi(x)$ (dashed) of beam node i . Additionally, the shape function of the displacement of node $i+1$ is sketched in gray.

Figure 3.4 Hermitian beam element (left) and shape functions for displacement and rotation (right).

Then a stacked vector of all catenary DoFs can be built:

$$\mathbf{Q} = \begin{bmatrix} \mathbf{Q}_{ca} \\ \mathbf{Q}_{co} \end{bmatrix}, \quad (3.15)$$

with which Eq. (3.13) can be elegantly written in matrix form (with sparsely populated system matrices since each element is only interacting with its neighbours):

$$\mathbf{M}\ddot{\mathbf{Q}} + \mathbf{D}\dot{\mathbf{Q}} + \mathbf{K}_e\mathbf{Q} = \mathbf{F}. \quad (3.16)$$

with the global mass matrix \mathbf{M} , damping matrix \mathbf{D} , and stiffness matrix \mathbf{K}_e . All external forces (e.g. pantograph, gravity) are considered in \mathbf{F} and a dot denotes derivatives w.r.t. time t .

The (nonlinear) coupling due to droppers between the carrier and contact wire as well as the coupling between the masts and the carrier wire are described by time-varying entries in the stiffness matrix that is a direct output of the FEM discretization process:

$$\mathbf{K}(t, \mathbf{Q}) = \mathbf{K}_e + \mathbf{K}_m(t) + \sum_{i=1}^{n_d} \mathbf{K}_{d,i}(t) \sigma(l_{d,i}(t) - l_{d,0,i}), \quad (3.17)$$

with \mathbf{K}_e as the stiffness matrix obtained during the FE discretization, see Eq. (3.16), and \mathbf{K}_m respectively \mathbf{K}_d contains the stiffness terms due to the masts and droppers, with the latter being active only when elongated as expressed with the Heaviside step function $\sigma(\bullet)$. The typical structure of $\mathbf{K}(t, \mathbf{Q})$ is shown in Figure 3.5 where all non-zero entries are marked with a dot and the off-diagonal entries stem from active (i.e. elongated) droppers.

The full FE nonlinear equation of motion for the whole catenary reads:

$$\mathbf{M}\ddot{\mathbf{Q}}(t) + \mathbf{D}\dot{\mathbf{Q}}(t) + \mathbf{K}(t, \mathbf{Q}(t))\mathbf{Q}(t) = \mathbf{F}(t, \mathbf{Q}(t)), \quad (3.18)$$

and dedicated time-integration schemes exist to solve these.

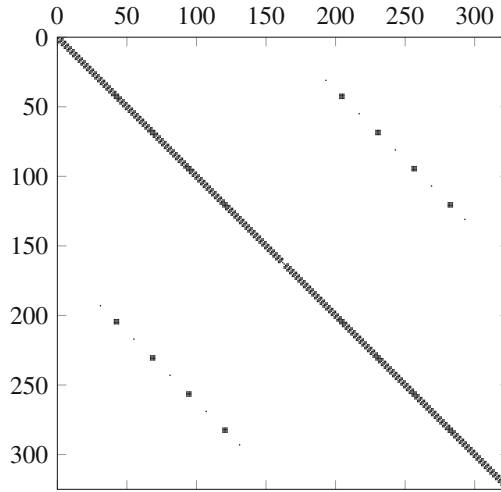


Figure 3.5 Typical structure of the sparse catenary stiffness matrix $\mathbf{K}(t, \mathbf{Q})$ that is obtained during the FE discretization process of the catenary dynamics.

3.1.3 Newmark Time-Integration

At the end of the FE discretization process, a set of coupled second-order ODEs (3.18) was obtained that still need to be solved in real-time. A widely used numerical integration scheme for FE-discretized PDEs are Newmark time-integration methods (solving with FDM (see Section 3.1.2.1) would theoretically also be possible).

As described in [4] the choice of the integrator is delicate. The dynamics of Eq. (3.18) describe lightly damped wave propagations with high stiffness elements (dropper and masts) and nonlinearities due to one-sided droppers. The integration time-step has to be sufficiently large to allow for real-time computation but still guarantee a stable and accurate simulation.

For the Newmark time-integration it is assumed that the DoF vectors \mathbf{Q} and $\dot{\mathbf{Q}}$ at the next time instant (corresponding to $t + \Delta t$) can be written as:

$$\mathbf{Q}_{k+1} = \mathbf{Q}_k + \Delta t \dot{\mathbf{Q}}_k + (\Delta t)^2 \left[\left(\frac{1}{2} - \beta_{\text{Nm}} \right) \ddot{\mathbf{Q}}_k + \beta_{\text{Nm}} \ddot{\mathbf{Q}}_{k+1} \right], \quad (3.19)$$

$$\dot{\mathbf{Q}}_{k+1} = \dot{\mathbf{Q}}_k + \Delta t \left[(1 - \gamma_{\text{Nm}}) \ddot{\mathbf{Q}}_k + \gamma_{\text{Nm}} \ddot{\mathbf{Q}}_{k+1} \right], \quad (3.20)$$

with parameters β_{Nm} and γ_{Nm} . Often, $\beta_{\text{Nm}} = 0.25$ and $\gamma_{\text{Nm}} = 0.5$ are used to avoid numerical damping and guarantee unconditional stability with linear time-invariant (LTI) system dynamics.

Plugging Eqs. (3.19)-(3.20) into the equations of motion (3.16) leads after rearrangements to the time integration update equations:

$$\mathbf{K}_{\text{DM},k} \ddot{\mathbf{Q}}_{k+1} = \tilde{\mathbf{F}}_{k+1}, \quad (3.21)$$

$$\mathbf{K}_{\text{DM},k} = \mathbf{K}_k(k\Delta t, \mathbf{Q}_k) \beta_{\text{Nm}} (\Delta t)^2 + \mathbf{D} \gamma_{\text{Nm}} \Delta t + \mathbf{M}, \quad (3.22)$$

$$\tilde{\mathbf{F}}_{k+1} = \mathbf{F}_{k+1} - \mathbf{D} \left[\dot{\mathbf{Q}}_k + \Delta t (1 - \gamma_{\text{Nm}}) \ddot{\mathbf{Q}} \right] - \mathbf{K}_k(k\Delta t, \mathbf{Q}_k) \left[\mathbf{Q}_k + \Delta t \dot{\mathbf{Q}}_k + (\Delta t)^2 \left(\frac{1}{2} - \beta_{\text{Nm}} \right) \ddot{\mathbf{Q}}_k \right]. \quad (3.23)$$

Equation (3.21) yields the acceleration vector at the next time instant from which via Eqs. (3.19) and (3.20) the velocity and displacements/rotations are directly obtained.

All operations in Eqs. (3.19)–(3.23) involve sparse matrices and vectors and can be carried out very efficiently. The inverse of $\mathbf{K}_{DM,k}$ in (3.21) (needed for solving for $\ddot{\mathbf{Q}}_{k+1}$) is not explicitly computed since highly sophisticated algorithms exist for solving this type of equation systems in linear runtime $\mathcal{O}(n)$, with n being the matrix dimension. On the other hand, solving a dense system of linear equations requires runtime $\mathcal{O}(n^2)$ which clearly has to be avoided in time-demanding real-time tasks.

The time-integrated dynamics for the special case of an LTI system can be written in standard explicit linear state-space form with the state vector:

$$\mathbf{x}_k = \begin{bmatrix} \mathbf{Q}_k \\ \dot{\mathbf{Q}}_k \end{bmatrix}. \quad (3.24)$$

However, in this case the system matrices become densely populated and incorporating the nonlinear dropper behavior is deemed laborious. Nevertheless, these considerations will become important in Section 3.1.6, when an absorbing boundary layer is derived by using an optimal control law.

3.1.4 Absorbing Boundaries for Partial Differential Equations

Standard boundary conditions of PDEs (e.g. Neumann or Dirichlet) lead to total wave reflections back into the computational domain and consequently for an undamped problem the energy inside the domain stays constant. However, as already described at the beginning of Section 3.1 an open domain solution with only a limited simulation domain is sought and thus the need for absorbing boundary conditions arises. These boundaries are transparent to outward traveling waves and ideally no wave reflections occur.

For a limited number of certain PDEs absorbing boundary conditions were already derived, e.g. for the two-dimensional wave equation in [5]. However, these analytical solutions are often limited to relatively simple PDEs, and for the (moving) EBB under axial pretension no absorbing boundary conditions could be found in literature and had to be developed.

Two different solution strategies were devised:

- an optimization-based approach where the values of an FD stencil are obtained by formulating an optimization problem,
- a controlled boundary layer, where forces and torques are applied at boundary nodes to dampen outward travelling waves.

Both methods are generically applicable to a wide range of PDEs that describe wave propagation phenomena and where a *dispersion relation* can be derived, which describes the connection between the spatial frequency $\omega_x \in \mathbb{R}$ and the temporal frequency $\omega_t \in \mathbb{R}$:

$$f(\omega_x, \omega_t) = 0. \quad (3.25)$$

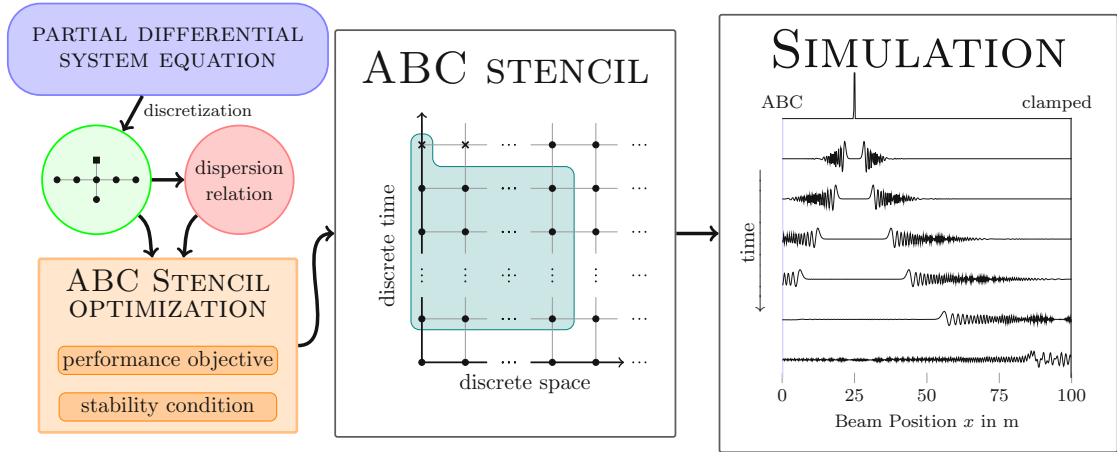


Figure 3.6 Graphical overview of the optimization-based approach for obtaining absorbing boundary stencil coefficients.

The dispersion relation can be obtained by plugging the harmonic wave solution:

$$\tilde{w}(x, t) = e^{i(\omega_x x + \omega_t t)} \quad (3.26)$$

into the PDE, e.g. (3.6) or (3.1). Likewise, by using the discrete version of Eq. (3.26):

$$\tilde{w}_k^j = (e^{i\omega_x \Delta x})^j (e^{i\omega_t \Delta t})^k \quad (3.27)$$

in the discretized PDE the *discrete dispersion relation* can be obtained.

3.1.5 Optimization-Based Approach

A graphical overview of the method is given in Figure 3.6. First, the PDE is discretized by the FDM (see Section 3.1.2.1) which yields a stencil for the inner nodes (exemplarily shown in the green circle of Figure 3.6). Then the discrete dispersion relation is computed and one out of two performance objectives has to be selected. After defining the boundary stencil size (generically shown in Figure 3.3 and the center of Figure 3.6) the optimization algorithm yields stencil coefficients realizing a stable absorbing boundary.

3.1.5.1 Performance Criterion

The performance criterion is based on simulating the harmonic wave solution (3.27) on a small test domain for several time steps with ABCs in place and then comparing the solution with the unbounded domain solution (by continuation of the harmonic wave). The initial condition is formed by the harmonic wave solution and then simulated forward by using the EBB stencil (sketched in green in Figure 3.3) respectively the boundary stencils (sketched in blue in Figure 3.3). The difference between both solutions (the simulated one and the unbounded domain's) can then be taken as an error measure:

$$e_{\text{OE}} = \sum_{n=2}^{N_t^{\text{OE}}} \sum_{k=2}^{N_x^{\text{OE}}} \|w_k^n - \tilde{w}_k^n\|, \quad (3.28)$$

where w_k^n are the results of the small-domain simulations, \tilde{w}_k^n are the harmonic wave solutions, N_t^{OE} is the number time steps of the simulation, and N_x^{OE} is the number of inner nodes that are evaluated by the OE-objective. The final OE-objective is then obtained by accumulating over different frequencies:

$$J_{\text{OE}} = \int_0^{\omega_{x,\text{max}}} w(\omega_x) e_{\text{OE}}(\omega_x) d\omega_x, \quad (3.29)$$

where $w(\omega_x)$ is a weighting function, used to emphasize the accuracy at frequencies of interests.

3.1.5.2 Stability Criterion

In general, even an allegedly well-performing ABC stencil can introduce long-term instabilities at certain frequencies and thus a dedicated stability criterion is introduced. A small test domain is defined with a few inner nodes and the ABCs in place. The dynamics are then formulated in state-space form (by using all node displacements of the previous time instants that are needed to compute the new values). Linear system dynamics analysis methods can then readily be applied and thus the eigenvalues of the system matrix can be investigated: the finite-difference scheme with ABCs in place is asymptotically stable if, and only if, all eigenvalues lie inside the unit circle, i.e. have a magnitude lower than one.

3.1.5.3 Results

In [Publication A] the performance of the proposed method was demonstrated on two simulation cases, with the first being an EBB under axial pretension, for which no absorbing boundaries have been derived before. The problem setup is depicted in Figure 3.7 (top). The dynamics of a very long beam could be simulated by applying ABCs. In the lower part of Figure 3.7 time snippets of the simulation are shown. At $t = T_1$ the simulation is started with an initial deflection of 0.5. In the next time instants dispersion phenomena are visible (frequency-dependent propagation speeds: lower frequencies travel slower) and between $T_2 < t < T_5$ the absorption of the first wave packets on the left boundary can be observed. Due to the clamped boundary condition on the right boundary, the waves are fully reflected back into the computational domain and are finally absorbed at $T_5 < t$.

The second simulation case is a two-dimensional wave equation, for which absorbing boundaries have already been analytically derived [5]. However, it was demonstrated that with the proposed method different characteristics could be tuned for, e.g. the incident angle of incoming waves or frequency weighting.

3.1.6 Control-Based Approach

The control-based approach for obtaining ABCs mimics the behavior of a so-called perfectly matched layer [6] by extending the original computational domain by boundary nodes (yellow area in Figure 3.2 respectively light gray area in Figure 3.8) on which forces

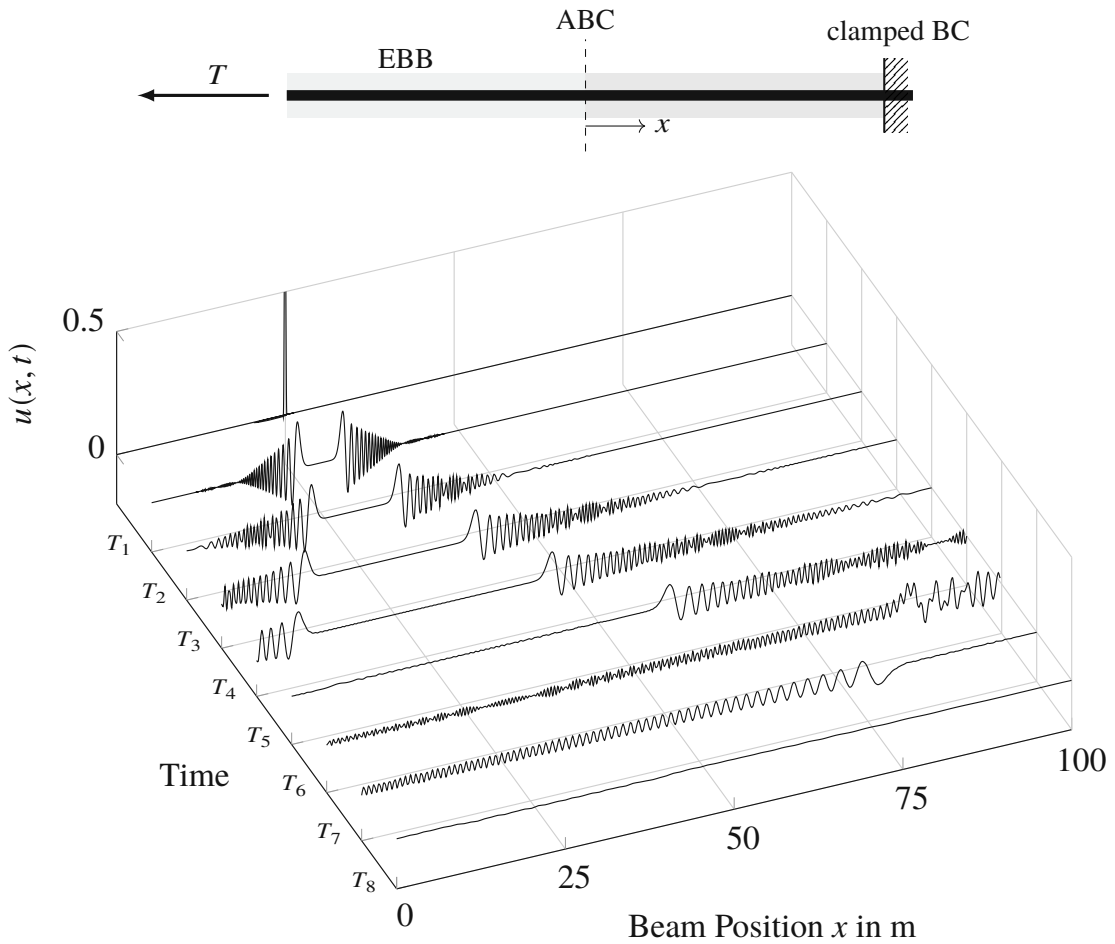


Figure 3.7 Setup of the simulation test case (top), where a part of an EBB (right half of the depicted beam) is simulated and the elongated domain dynamics are obtained by placing ABCs on the left boundary. In the lower part, time snippets of the simulation are shown: The initial deflection is split in two wave packets which are either reflected (right boundary) or absorbed (left boundary).

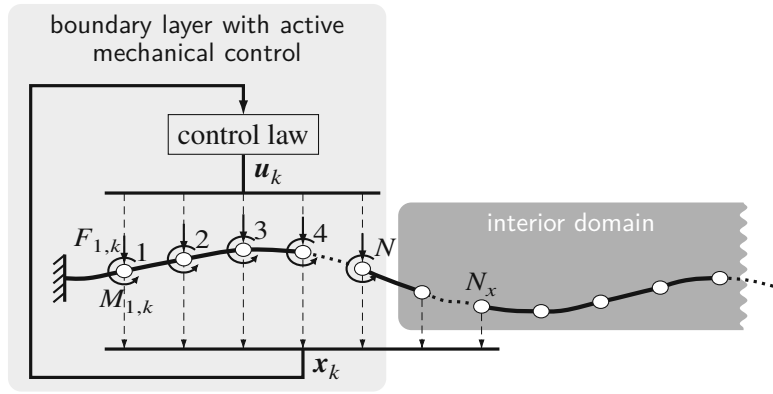


Figure 3.8 Overview of the control-based approach for realizing ABCs: The original computational domain is extended by a layer in which forces (and torques) are applied by using a control law such that outward traveling waves are attenuated.

and torques are applied by a control law. This method was first described in [7] for FD-discretized dynamics. A detailed derivation of this method (for FE dynamics) and further investigations on the role of the (discretized) dispersion relation can be found in [Publication C] and [Publication D].

The proposed method is divided in four steps which are briefly sketched in the following sub-chapters:

- Extension of the computational domain (with the nodes of the controlled boundary layer)
- Modal approximation of the wave field
- Construction of the reference solution (based on the harmonic wave approximation)
- Formulation of the control problem (position tracking of the reference solution)

3.1.6.1 Extension of the Computational Domain

First, the original domain is extended by controlled boundary nodes (light gray area in Figure 3.8) and the resulting DoFs of the new beam are collected into a vector \mathbf{Q} . Then the dynamics of the beam (or just the first N_x nodes) are written in state-space form by using the state-vector defined in Eq. (3.24):

$$\begin{aligned} \mathbf{x}_{k+1} &= \mathbf{A}\mathbf{x}_k + \mathbf{B}\mathbf{u}_k \\ \mathbf{y}_k &= \mathbf{C}\mathbf{x}_k, \end{aligned} \quad (3.30)$$

where the control inputs are the forces and torques in the boundary layer nodes:

$$\mathbf{u}_k = [F_{1,k} \quad M_{1,k} \quad F_{2,k} \quad \dots \quad M_{N-1,k} \quad F_{N,k} \quad M_{N,k}]^T. \quad (3.31)$$

3.1.6.2 Modal Approximation of the Wave Field

At each time instant, the wave field (displacement and rotation) of the first N_x nodes (see Figure 3.8) is then approximated by a sum of sine and cosine waves (to express phase shifts) with different frequencies and amplitudes, where the amplitudes of the trigonometric functions are obtained via a least-squares approximation:

$$\mathbf{g}_k = (\mathbf{L}^T \mathbf{L} + \boldsymbol{\alpha})^{-1} \mathbf{L}^T \mathbf{Q}_k = \mathbf{K}_{\text{mod}} \mathbf{x}_k, \quad (3.32)$$

with \mathbf{g}_k being a matrix of stacked amplitudes of the harmonic waves for the different frequencies, $\boldsymbol{\alpha}$ a diagonal regularization matrix, and \mathbf{L} as a collection of constant coefficients for the sine and cosine waves for the DoFs of each node. The DoFs of the first N_x nodes of the beam can now be approximated in modal coordinates:

$$\widehat{\mathbf{Q}}_k = \mathbf{L} \mathbf{g}_k \approx \mathbf{Q}_k. \quad (3.33)$$

3.1.6.3 Construction of the Reference Solution

Now that the DoFs of the first N_x nodes can be approximated by Eq. (3.33) in modal coordinates, a reference solution for the controller can be derived. The (undamped) beam dynamics can be predicted for an arbitrary time instant $k + l$ by defining shifting matrices, e.g. for the displacement DoFs and the frequency $\omega_{x,i}$:

$$\mathbf{T}_{i,l}^w = \begin{bmatrix} \cos(\omega_{x,i} \Delta x + al) & \sin(\omega_{x,i} \Delta x + al) \\ \cos(\omega_{x,i} 2\Delta x + al) & \sin(\omega_{x,i} 2\Delta x + al) \\ \vdots & \vdots \\ \cos(\omega_{x,i} N\Delta x + al) & \sin(\omega_{x,i} N\Delta x + al) \end{bmatrix}, \quad (3.34)$$

where the dispersion relation is used to calculate $\omega_{t,i}$ and subsequently the frequency-dependent phase shift due to elapsed time: $al = \omega_{t,i} l \Delta t$. The displacement field at time instant $k + l$ can then be calculated as a summation of all frequency contributions:

$$\widehat{\mathbf{w}}_{k+l} = \sum_{i=1}^{N_\Omega} \mathbf{T}_{i,l}^w \mathbf{g}_{i,k}. \quad (3.35)$$

A reference trajectory can now easily be obtained by introducing a damping matrix \mathbf{D} in Eq. (3.35):

$$\mathbf{D}^w = \text{diag}(e^{-\sigma_w(0)}, e^{-\sigma_w(\Delta x)}, \dots, e^{-\sigma_w(N_x \Delta x)}), \quad (3.36)$$

where $\sigma_w(x)$ is used to realize a desired damping profile, i.e. zero inside the original interior domain and rapidly growing in the boundary layer.

By additionally incorporating the rotational DoFs, the reference solution for the next n_p time instants can be written as:

$$\mathbf{Y}_{\text{ref},k} = \mathbf{T} \mathbf{g}_k = \mathbf{T} \mathbf{K}_{\text{mod}} \mathbf{x}_k \quad (3.37)$$

where $\mathbf{Y}_{\text{ref},k}$ consists of the reference vectors of the next n_p time instants and the damping matrices $\mathbf{D}^{w/\varphi}$ are already incorporated in \mathbf{T} .

3.1.6.4 Formulation of the Control Problem

Now that a reference trajectory over the next n_p time instants can efficiently be computed by a vector/matrix multiplication with Eq. (3.37) a quadratic cost function is defined that penalizes the control error as well as the control inputs:

$$J = \sum_{j=k+1}^{k+n_p} \|\mathbf{y}_{\text{ref},j} - \mathbf{y}_j\|_{\mathcal{Q}_{\text{ABC}}}^2 + \sum_{j=k}^{k+n_c-1} \|\mathbf{u}_j\|_{\mathcal{R}_{\text{ABC}}}^2. \quad (3.38)$$

\mathcal{Q}_{ABC} and \mathcal{R}_{ABC} are weighting matrices that are used to penalize the applied forces and torques relative to the position and rotation errors. Minimizing Eq. (3.38) by setting its first derivative to zero eventually leads to a linear state-feedback law of the form:

$$\mathbf{u}_k = \mathbf{K}_{\text{ABC}} \mathbf{x}_k. \quad (3.39)$$

Equation (3.39) is evaluated in each time-step and the resulting control input \mathbf{u}_k (consisting of forces and torques) is directly applied to the boundary nodes, eventually realizing the desired wave absorption behavior.

3.1.6.5 Results

In Figure 3.9 some simulation details are shown where a moving EBB under axial pretension is simulated on a practically unbounded domain (black, dashed) with no influences of the domain boundaries on the simulation results and on a shortened domain with controlled boundary layers in place (gray, solid). Additionally, in the upper plot, the fading of the dropper stiffness in the real-time catenary model is visualized (blue, dash-dotted) and a spring is moving through the computational domain to demonstrate partial reflections appearing on droppers (2nd and 3rd subplot). Outward traveling waves are well attenuated inside the boundary region and in the last two subplots, the job of the controller is clearly visible when both simulations (unbounded vs. limited domain) can be easily compared to each other. No visible dynamics remain inside the inner domain after the wave packets hit the boundaries.

3.1.7 Summary of Catenary Modeling

The modeling of the catenary as described in Section 3.1 was based on physical considerations and so a white-box model of the complex catenary dynamics could be obtained that is applicable to a wide range of different catenaries by directly changing the physical parameters (e.g. wire cross-section, tension force, ...). Special cases like multi-traction operation, nonlinear pantograph models, or catenary span transitions can also be examined with the current approach.

However, to derive a real-time capable catenary model a coordinate transformation is introduced so that the pantograph as the UUT is fixed in the computational domain and the catenary is now moving. With this approach, the computational domain can be drastically reduced by only investigating the dynamics in the vicinity of the pantograph. However,

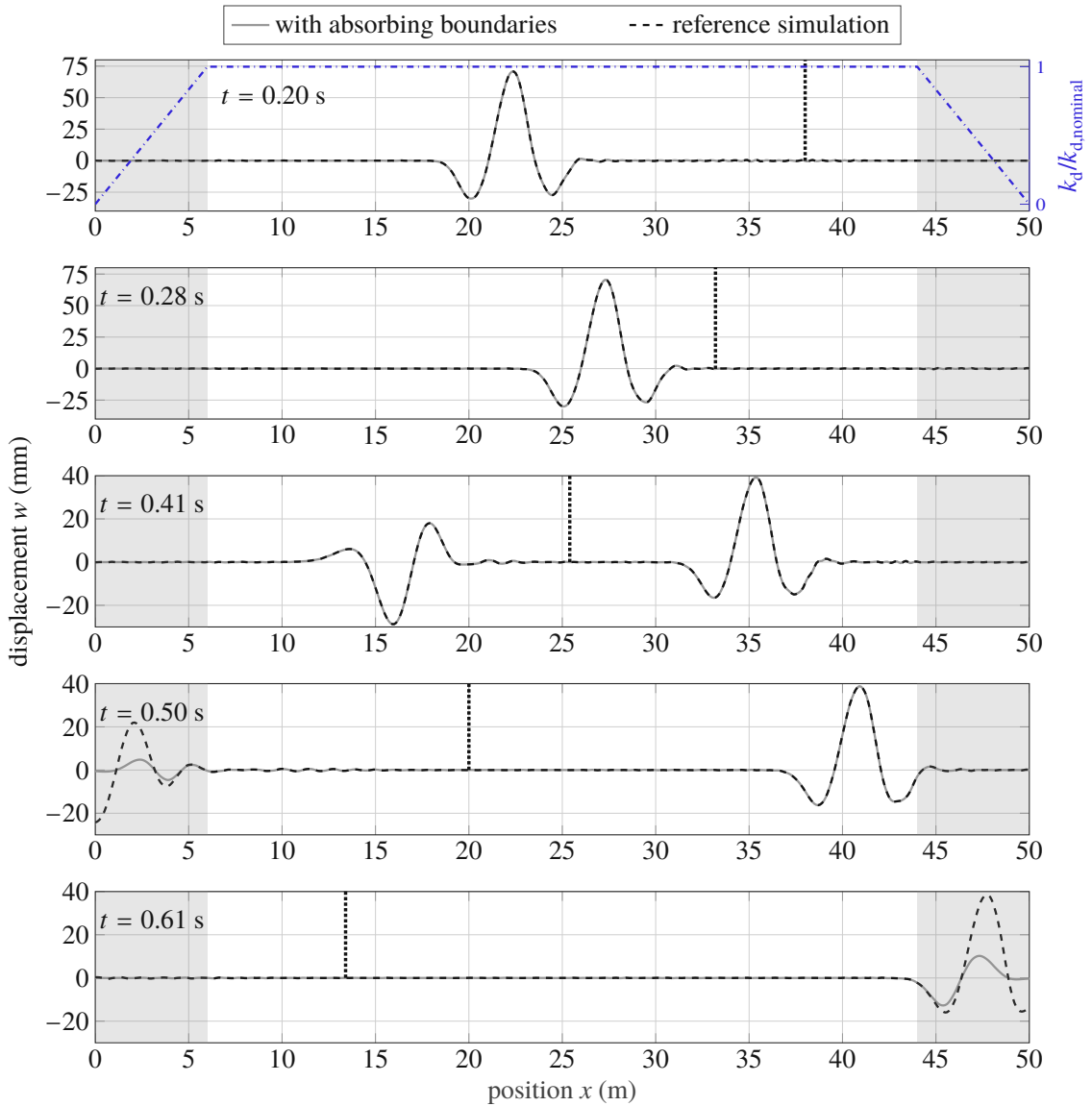


Figure 3.9 Simulation study of a moving EBB under axial pretension with controlled boundary layers according to Section 3.1.6 on both sides (gray area). Additionally, a dropper is moving through the computational domain (vertical dashed line) and in the upper plot it is shown in blue how the dropper stiffness is linearly faded in/out inside the boundary layers. The simulation on the truncated domain is shown in a gray solid line while the reference simulation on a practically unbounded domain is shown in dashed black.

wire	ρA (kg/m)	β (Ns/m)	EI (Nm ²)	T (N)		
carrier	1.07	0.6	100	16e3		
contact	1.35	0.2	150	20e3		
dropper	1	2	3	4	5	... 9
$x_{d,i}$ (m)	5	10.5	17	23.5	30	symmetric
$l_{d,0,i}$ (m)	0.845	0.625	0.515	0.515	0.625	symmetric
	β_{Nm}	γ_{Nm}	Δt	Δx	n_{spans}	
catenary-fixed	0.25	0.5	0.2 ms	0.25 m	28	
pantograph-fixed	0.255	0.525	2.2 ms	1.00 m	2	

Table 3.1 Physical and simulation parameters of both catenary systems (reference and real-time simulation)

one problem emerges: the treatment of the boundaries of the computational domain, as standard boundary conditions lead to unphysical wave reflections back into the domain. This was solved by deriving absorbing boundaries using two different approaches.

3.1.8 Results

The real-time capable catenary simulation is compared with the results obtained from a very high-fidelity catenary simulation in fixed coordinates with a much finer temporal and spatial discretization. Table 3.1 summarizes the catenary and simulation parameters.

Figure 3.10 shows the results of both simulations (displacement, contact force, and force spectra). In both simulations a generic three-mass-oscillator was used as the pantograph model and the agreement between both models' output is evident, as can be seen from the displacement and force snapshots or from the spectrogram (third subplot) over a longer 6 s period (time needed to pass 7 catenary spans at a velocity of 250 km/h).

While the low-frequency contributions are in very good agreement, the high-frequency contents on the real-time model tend to be higher. This probably stems from non-optimal performance of the boundary layer and the emerging dropper stiffnesses (even though a linear fading as shown in Figure 3.9 was used).

3.1.9 Simplified Catenary Model for Linear Control Design

Even though the nonlinear reduced high-fidelity model is computable in real-time, it is not directly applicable in classic linear control systems theory and also not in the (integrated) impedance control concept described in Section 3.2.1. Due to time-dependencies (moving droppers and masts) as well as the nonlinearities (one-sided droppers) the catenary model can not be formulated as a linear time invariant (LTI) state-space model.

Therefore, a reduced catenary model that is initialized in each time instant by the states of the nonlinear real-time catenary model is needed. For this reduced model it is assumed that all droppers are slackened and can thus be omitted. This is especially true in the

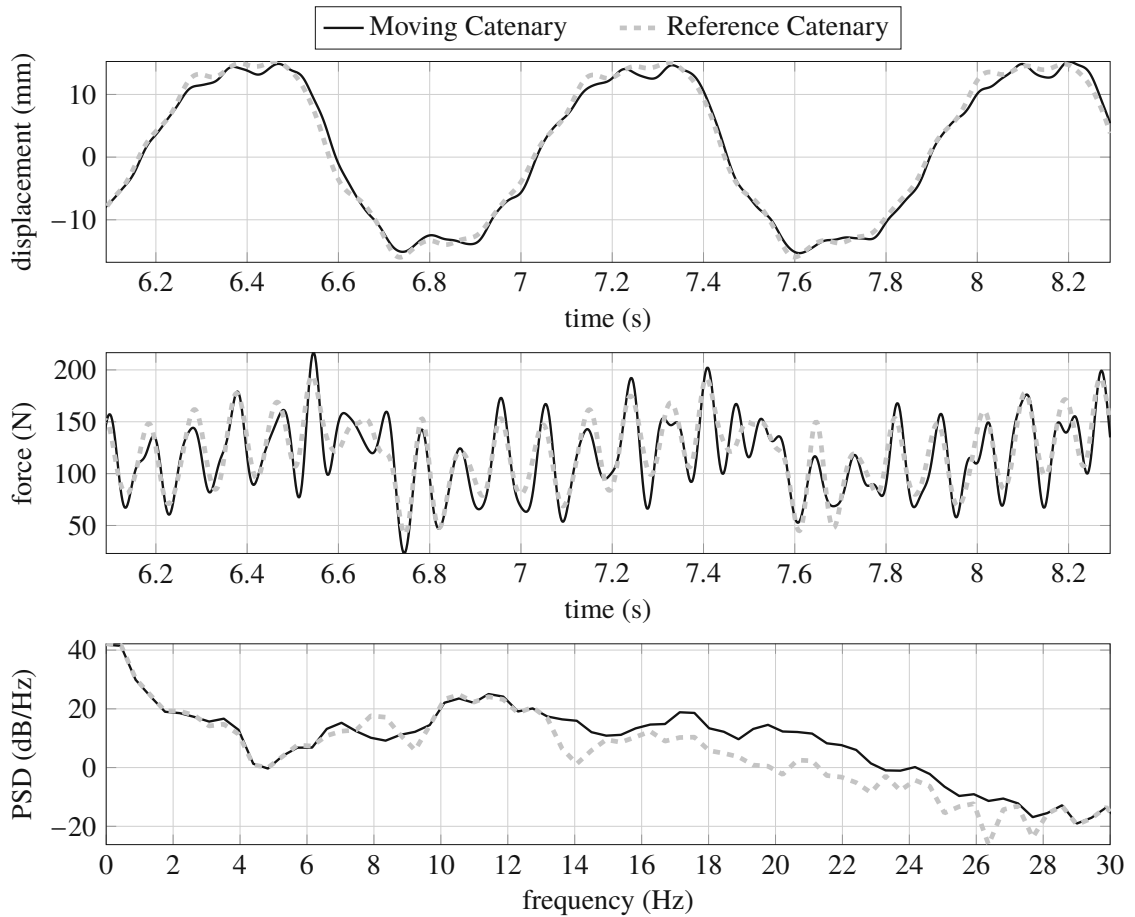


Figure 3.10 Comparison of simulation results of the real-time catenary model (black, solid) with a high-fidelity reference simulation (gray dashed). A 3-DoF-oscillator was used as a pantograph model in both cases. The first two plots show the displacement of the pantograph's contact point and the resulting force while the third plot shows a spectrogram of the force signal over a longer 6 s period.

vicinity of the pantograph since it normally pushes the contact wire upwards. Because of the omitted droppers, there is no coupling to the carrier wire which can therefore be omitted too. The reduced catenary model used for the impedance control design consists of just the contact wire. Depending on the length of the modeled catenary, it may be advantageous to only consider a segment around the pantograph.

The dynamics of the reduced model can then be formulated in linear state-space form:

$$\begin{aligned}\hat{\mathbf{x}}_{\text{cat}}(k+1) &= \mathbf{A}_{\text{cat}}\hat{\mathbf{x}}_{\text{cat}}(k) + \mathbf{B}_{\text{cat}}u_{\text{cat}}(k), \\ \hat{\mathbf{y}}_{\text{cat}}(k) &= \mathbf{C}_{\text{cat}}\hat{\mathbf{x}}_{\text{cat}}(k) = \begin{bmatrix} w_{\text{cat}}(k) \\ \dot{w}_{\text{cat}}(k) \end{bmatrix}.\end{aligned}\quad (3.40)$$

The states $\hat{\mathbf{x}}_{\text{cat}}(k)$ of the simplified model are initialized in each time-step by using the states of the fully nonlinear catenary model which is simulated in parallel:

$$\hat{\mathbf{x}}_{\text{cat}}(k) = \hat{\mathbf{f}}(\mathbf{x}_{\text{cat}}(k)). \quad (3.41)$$

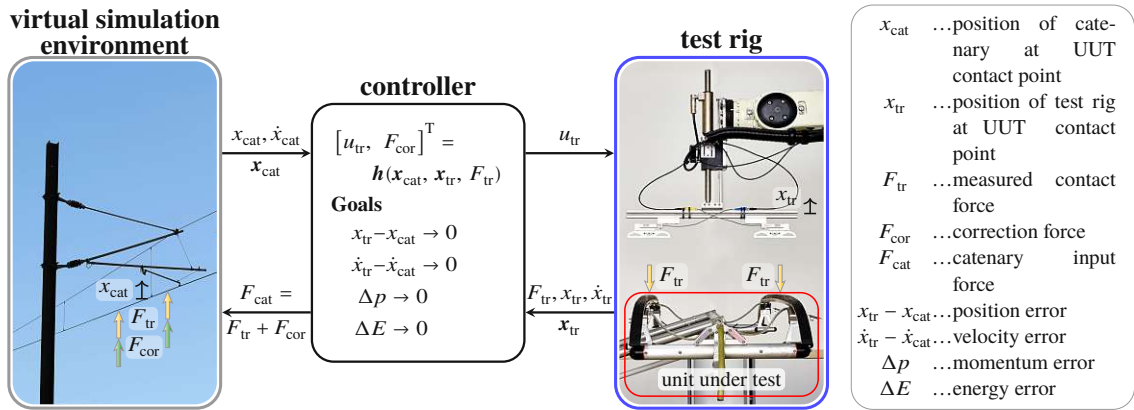


Figure 3.11 Information flow in the PHiL catenary emulation on the test rig.

3.2 Test Rig Impedance Control

The basic information flow of the catenary emulation control concept is sketched in Figure 3.11. At the heart (depicted at the center) the controller of the integrated impedance control (IIC) concept manages the information flow between the catenary model and the test rig. It incorporates a simplified catenary model as well as a model of the (already position-controlled) test rig (all in the same time-base). The primary goal of the model predictive IIC is to output control inputs u_{tr} to the faster inner position-tracking test rig control loop such that the catenary dynamics are emulated on the test rig. As a second control task it utilizes a virtual correction force F_{cor} to the catenary model to drive the momentum and energy errors in the PHiL run to zero. It thus has the ability to influence both dynamics, the test rig's as well as the catenary's.

3.2.1 Test Rig Control

The control loop of the test rig is a position-tracking of the linear drive's slider displacement. The underlying model is made up of the principle of linear momentum of the slider:

$$m\ddot{w}_{tr} = K_f i_{dmd} - mg - F_{cogging} - F_{friction} - F_d, \quad (3.42)$$

with m being the slider's mass, w_{tr} its displacement, K_f the motor force constant, i_{dmd} the motor demand current (control input), g the gravitational constant, $F_{cogging}$ the cogging force due to the permanent magnets in the slider, $F_{friction}$ as the friction force, and F_d as unmodeled disturbance forces (estimated by an observer).

Additionally, some resonant frequencies of the test rig structure (industrial robot) were partly excited by the test rig control and even amplified as these frequencies also appeared in the force signal that eventually got fed into the catenary model. To prevent these frequencies from appearing in the generated control input, the design plant of the test rig model was modified to include a second output (besides the slider's displacement), namely a frequency weighting of i_{dmd} . Figure 3.12 visualizes the modified design plant. The filter

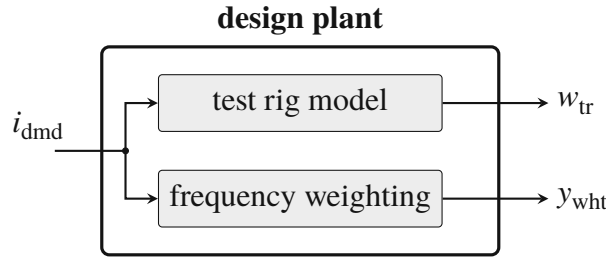


Figure 3.12 Modified design plant of the inner test rig control loop (the linear drive’s slider displacement) that now additionally includes a frequency weighting of the control input.

function for the frequency weighting was chosen to:

$$G_{\text{freq. weighting}} = \frac{s\omega}{s^2 + 2s\zeta\omega + \omega^2} \quad (3.43)$$

with the unwanted frequency ω and a damping factor ζ .

A standard LQR control law was used on the design plant of Figure 3.12 with Eqs. (3.42) and (3.43) with a sampling rate of $T_{s,\text{fast}} = 1/5000$ s.

The closed-loop position-tracking dynamics can then be formulated in a slower time-base $T_{s,\text{tr}} = T_{s,\text{cat}} = 1/500$ s as PT2 behavior in state-space form:

$$\begin{aligned} \mathbf{x}_{\text{tr}}(k_{\text{tr}} + 1) &= \mathbf{A}_{\text{tr}}\mathbf{x}_{\text{tr}}(k_{\text{tr}}) + \mathbf{B}_{\text{tr}}w_{\text{tr,ref}}(k_{\text{tr}}), \\ \mathbf{y}_{\text{tr}}(k_{\text{tr}}) &= \mathbf{C}_{\text{tr}}\mathbf{x}_{\text{tr}}(k_{\text{tr}}) = \begin{bmatrix} w_{\text{tr}}(k_{\text{tr}}) \\ \dot{w}_{\text{tr}}(k_{\text{tr}}) \end{bmatrix}, \end{aligned} \quad (3.44)$$

The control input $w_{\text{tr,ref}}$ is then the output of the impedance controller and is used as a reference position for the faster position-tracking inner test rig control loop that eventually generates the current demand value to the linear drive.

3.2.2 Conserved Quantities

During an actual train ride there is a permanent exchange of momentum and energy between the pantograph and the catenary. In order to obtain physical trustworthy results in PHiL testing the impedance model dynamics (in this case the catenary) needs to be accurately tracked by the test rig and imposed to the UUT. There is a permanent exchange of power signals and consequently physical conservation laws have to be taken into account as well because momentum and energy is transferred at two interfaces:

- between the test rig and the UUT,
- from the UUT to the catenary model.

This is visualized in Figure 3.13 where both power flows are sketched and ideally, these quantities are consistent. Otherwise, it may for example be possible that on average more energy is transferred into the impedance model than is actually exchanged between the

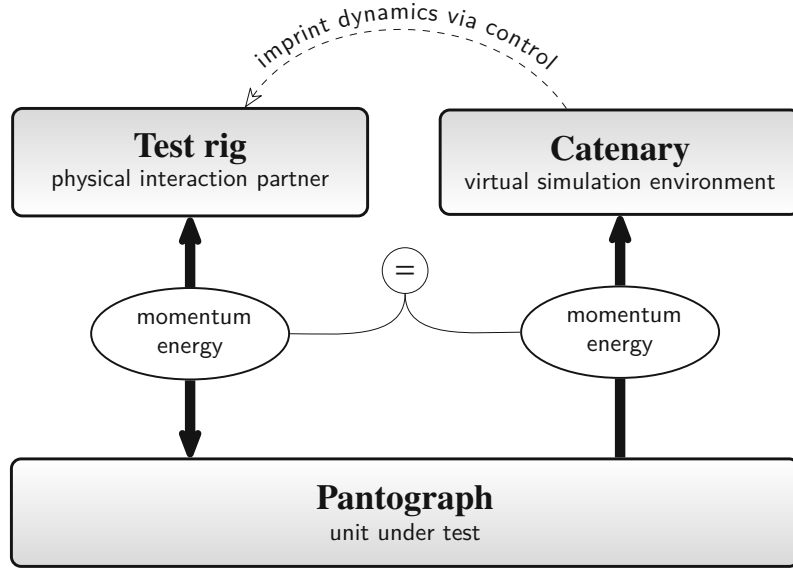


Figure 3.13 The catenary dynamics are emulated on the test rig, leading to a momentum and energy exchange between the pantograph and the test rig. Since the measured contact force is taken as an input value to the catenary model, momentum and energy is also transferred into the catenary model. Ideally, the values of these exchanged conserved quantities at both interfaces are equal.

UUT/test rig interface which may lead to inaccurate results (e.g. increased fuel consumption in combustion engine PHiL testing as demonstrated in [8]).

To ensure consistency, the controller is not only allowed to utilize the test rig actuation but also modify the measured contact force that is fed into the catenary model by an additive correction force F_{cor} :

$$F_{\text{cat}}(k) = F_{\text{tr}}(k) + F_{\text{cor}}(k), \quad (3.45)$$

where F_{cat} is the force that is fed into the catenary simulation and F_{tr} is the measured contact force at the test rig. By utilizing F_{cor} the controller can ensure its second goal (the first being impedance tracking): momentum and energy conservation/consistency by keeping the cumulated difference between $E_{\text{tr}}(k)$ (the energy exchanged at the test rig) and $E_{\text{cat}}(k)$ (the one transferred into the catenary model) small:

$$\begin{aligned} \Delta E(k) &= E_{\text{tr}}(k) - E_{\text{cat}}(k), \\ E_{\text{tr}}(k) &= \sum_{j=0}^k T_s F_{\text{tr}}(j) \dot{w}_{\text{tr}}(j), \\ E_{\text{cat}}(k) &= \sum_{j=0}^k T_s (F_{\text{tr}}(j) + F_{\text{cor}}(j)) \dot{w}_{\text{cat}}(j). \end{aligned} \quad (3.46)$$

Equation (3.46) shows that F_{cor} can be used to reduce the energy error but on the other

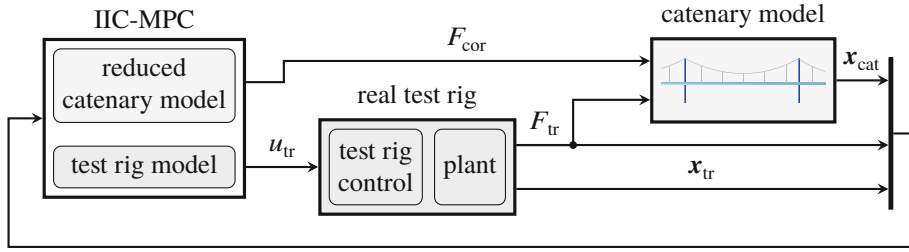


Figure 3.14 Overall control structure of the catenary emulation on the test rig.

hand the introduction of the correction force leads to a momentum error:

$$\begin{aligned}
 \Delta p(k) &= p_{tr}(k) - p_{cat}(k) \\
 &= \sum_{j=0}^k T_s F_{tr}(j) - \sum_{j=0}^k T_s (F_{tr}(j) + F_{cor}(j)) \\
 &= \sum_{j=0}^k T_s F_{cor}(j).
 \end{aligned} \tag{3.47}$$

While the minimization of the momentum error (3.46) can be directly incorporated into classic linear feedback control design methods, the energy error is a nonlinear term due to the multiplication of velocity (a state of the system) and force (a model input).

As outlined in [Publication B] constraints on the correction force F_{cor} were re-formulated in each time step such that a reduction of energy error is obtained:

$$|\Delta E(k)| \leq |\Delta E(k-1)|. \tag{3.48}$$

Depending on the sign of $\dot{w}_{cat}(k)$ and $\Delta E(k-1)$ different expressions for the upper and lower bounds of the correction force result, e.g. for $\dot{w}_{cat}(k) > 0$ and $\Delta E(k-1) > 0$:

$$\begin{aligned}
 F_{cor}^-(k) &= \frac{(1-\alpha)\Delta E(k-1)}{\dot{x}_{cat}(k)T_s} + F_{tr}(k) \left(\frac{\dot{x}_{tr}(k)}{\dot{x}_{cat}(k)} - 1 \right), \\
 F_{cor}^+(k) &= \frac{\Delta E(k-1)}{\dot{x}_{cat}(k)T_s} + F_{tr}(k) \left(\frac{\dot{x}_{tr}(k)}{\dot{x}_{cat}(k)} - 1 \right),
 \end{aligned} \tag{3.49}$$

with $0 < \alpha < 1$ being a user-chosen constant that describes the decay rate of the energy error. Applying a correction force in between those bounds leads to a decay in energy error. Additionally, different robustification heuristics were developed in order to guarantee a small overall error in energy and momentum transfers as well as minimal impact on the catenary dynamics.

3.2.3 Impedance Control

Figure 3.14 depicts a block diagram of the implemented control structure. A model predictive controller is used in an integrated impedance control (IIC) architecture, meaning that

the controller incorporates models of the virtual simulation environment (here a simplified catenary model) and the test rig. In contrast to the classic cascaded impedance control structure, where just a reference signal for the underlying position tracking control is generated, the IIC structure allows for lag-free impedance tracking due to its model-based predictive nature. Additionally, as already outlined in Section 3.2.2, a second control input is introduced where the controller gains direct access to the catenary model excitation via a virtual correction force F_{cor} that is used to keep the conserved quantities energy and momentum consistent throughout the PHiL test run.

The state vector of the design plant consists of the state vectors of a test rig model (in this case a PT2 position tracking model of the closed inner test rig control loop (described in Section 3.2.1, Eq. (3.44)), the simplified catenary model described in Section 3.1.9 and the momentum error (3.47):

$$\mathbf{x}(k) = [\mathbf{x}_{\text{tr}}^{\text{T}}(k) \quad \hat{\mathbf{x}}_{\text{cat}}^{\text{T}}(k) \quad \Delta p(k)]^{\text{T}}. \quad (3.50)$$

With this state vector the following state-space system as the controller's design plant is constructed:

$$\begin{aligned} \mathbf{x}(k+1) &= \mathbf{A}\mathbf{x}(k) + \mathbf{B}\mathbf{u}(k) + \mathbf{E}z(k), \\ \mathbf{y}(k) = \mathbf{C}\mathbf{x}(k) &= \begin{bmatrix} e_{\text{pos}}(k) \\ e_{\text{vel}}(k) \\ \Delta p(k) \end{bmatrix} = \begin{bmatrix} w_{\text{tr}}(k) - w_{\text{cat}}(k) \\ \dot{w}_{\text{tr}}(k) - \dot{w}_{\text{cat}}(k) \\ \Delta p(k) \end{bmatrix}, \end{aligned} \quad (3.51)$$

with e_{pos} and e_{vel} being the position and velocity errors of the test rig dynamics to the catenary's dynamics. The control inputs are $u_{\text{tr}}(k)$ as a reference trajectory to the underlying test rig position tracking loop respectively $F_{\text{cor}}(k)$ as the virtual correction force. The disturbance input z is the measured contact force on the test rig $F_{\text{tr}}(k)$:

$$\mathbf{u}(k) = \begin{bmatrix} u_{\text{tr}}(k) \\ F_{\text{cor}}(k) \end{bmatrix}, \quad z(k) = F_{\text{tr}}(k). \quad (3.52)$$

The system matrices in Eq. (3.51) are built as follows:

$$\begin{aligned} \mathbf{A} &= \begin{bmatrix} \mathbf{A}_{\text{tr}} & \mathbf{0} & \mathbf{0} \\ \mathbf{0} & \mathbf{A}_{\text{cat}} & \mathbf{0} \\ \mathbf{0} & \mathbf{0} & 1 \end{bmatrix}, \quad \mathbf{B} = \begin{bmatrix} \mathbf{B}_{\text{tr}} & \mathbf{0} \\ \mathbf{0} & \mathbf{B}_{\text{cat}} \\ \mathbf{0} & T_s \end{bmatrix}, \\ \mathbf{E} &= \begin{bmatrix} \mathbf{0} \\ \mathbf{B}_{\text{cat}} \\ 0 \end{bmatrix}, \quad \mathbf{C} = \begin{bmatrix} \mathbf{C}_{\text{tr}} & -\mathbf{C}_{\text{cat}} & \mathbf{0} \\ \mathbf{0}^{\text{T}} & \mathbf{0}^{\text{T}} & 1 \end{bmatrix}. \end{aligned} \quad (3.53)$$

A vector of future control moves is defined:

$$\mathbf{U} = [\mathbf{u}^{\text{T}}(k) \quad \mathbf{u}^{\text{T}}(k+1) \quad \dots \quad \mathbf{u}^{\text{T}}(k+N_c-1)]^{\text{T}} \quad (3.54)$$

with N_c being the control horizon. A model predictive controller is then designed to calculate the next N_c control moves in each time instant anew. Therefore, a quadratic cost

function is defined that penalizes the control error up to a prediction horizon N_p as well as the upcoming control moves via weighting matrices \mathbf{Q} and \mathbf{R} :

$$J(\mathbf{U}, \mathbf{x}, k) = \sum_{i=1}^{N_p} \mathbf{x}^T(k+i) \mathbf{Q} \mathbf{x}(k+i) + \sum_{i=0}^{N_c-1} \mathbf{u}^T(k+i) \mathbf{R} \mathbf{u}(k+i). \quad (3.55)$$

Because of test rig limitations and, more importantly, to impose bounds on F_{cor} (see Section 3.2.2) a constrained optimization problem is formulated to obtain the vector of future control moves:

$$\begin{aligned} \mathbf{U}^* &= \arg \min_{\mathbf{U}} J(\mathbf{U}, \mathbf{x}(k), k) \\ &\text{subject to } \mathbf{M}_{\mathbf{U}} \mathbf{U} \leq \boldsymbol{\gamma}_u, \text{ and} \\ &\mathbf{M}_{\mathbf{x}} \mathbf{X} \leq \boldsymbol{\gamma}_x, \end{aligned} \quad (3.56)$$

where \mathbf{X} is the stacked vector of the states from time instant k to $k + N_p - 1$ (analogous to Eq. (3.54)) and $\mathbf{M}_{\mathbf{x}}$ and $\mathbf{M}_{\mathbf{U}}$ are matrices used to formulate linear state and input constraints. Although the optimization problem (3.56) is convex, in general, a closed-form solution can not be directly obtained but iterative solvers have to be used.

	core 1	core 2	core 3
tasks	data acquisition	catenary simulation	impedance MPC
sampling frequency	5 kHz	500 Hz	500 Hz
turnaround time	0.05 ms	0.33 ms	1.77 ms
memory usage	5.0 MB	7.2 MB	7.0 MB

Table 3.2 Utilization of the real-time platform cores during the test runs

3.3 Results of the Test Rig Catenary Emulation

The high-fidelity nonlinear catenary model developed in Section 3.1 is used in combination with the model predictive impedance controller described in Section 3.2.3 to finally emulate the catenary dynamics on a full-scale PHiL test rig.

3.3.1 Implementation Details

A dSPACE ds1006 real-time computer comprising a quad-core 2.8 GHz processor was used for test rig control and catenary simulations. Table 3.2 gives an overview of the three cores used and how they are utilized. In detail, the cores of the real-time computer were utilized as follows:

Core 1 – data acquisition and test rig control The task on this core was set to a sampling frequency of 5 kHz to match the linear drive’s frequency with which motor current demand values are internally processed, and the basic test rig position tracking controller described in Section 3.2.1 is placed in this task. The reference position for this controller is calculated on core 3 (“impedance MPC”) and transferred to the faster time base by linearly interpolating between the first two calculated control inputs ($u_{tr}(k)$ and the prediction of $u_{tr}(k + 1)$, the control input at the upcoming time instant).

Data acquisition of all measurements and the observer for the linear drive’s states and the contact force (including its low-pass filter) are placed there. Additionally, some high-level control tasks (like switching the impedance model or enabling different operating modes like position tracking or impedance tracking) are done here.

Core 2 – catenary simulation The nonlinear catenary simulation as described in Section 3.1 is exclusively computed on this core. A low-pass-filtered/estimated value of the measured contact force (possibly corrected by F_{cor}) serves as the input to this model.

For efficiently calculating the sparse-matrix algebra emerging in the time-integration process (see Section 3.1.3) the C++ linear-algebra library Eigen [9] was used and the rest of the catenary simulation was programmed in C++ too.

The output of this core's task is the high-fidelity nonlinear catenary simulation, respectively the state vector of the reduced model used in the impedance MPC on core 3, see Eq. (3.41).

Core 3 – impedance MPC The model predictive impedance controller described in Section 3.2.3 operates on this core with the same sampling frequency of 500 Hz as the nonlinear catenary model of core 2.

The test rig states of the control model are initialized with the observer states from core 1 while the catenary states of the reduced model are calculated on core 2, see Eq. (3.41).

For solving the constrained MPC optimization problem (3.56) the iterative solver qpOASES [10] was used that is based on an active set method [11]. The implemented constraints were test rig displacement limitations as well as bounds imposed on the correction force F_{cor} to reduce the energy error.

The memory usage on each core shows a quite uniform utilization, demonstrating one of the advantages of sparse algebra since only the non-zero matrix entries are stored and thus a small memory footprint results. The short turnaround time on core 2 indicates that even more catenary spans or a finer discretization could be used in future PHiL runs to further increase the model's fidelity.

3.3.2 Results

A virtual train ride with a travel speed of 250 km/h and the parameters from Table 3.1 (slightly modified to $\Delta x = 1.25$ m, and $\beta = 0$) is emulated on a full-scale pantograph test rig (Figure 1.1) and a physical pantograph is put in interaction with a virtual catenary.

Figure 3.15 shows a 2.5 s snapshot of the PHiL test. The upper part shows the displacement of the catenary at the pantograph's contact point (the drop in the mean displacement is caused by a manual reduction of the pressure inside the pantograph's actuation during the test run) as well as the resulting contact force and its power spectrum density. The catenary dynamics are overall very well tracked. The high-frequency disturbances stem from test rig vibration modes that are induced into the catenary simulation via the contact force measurements.

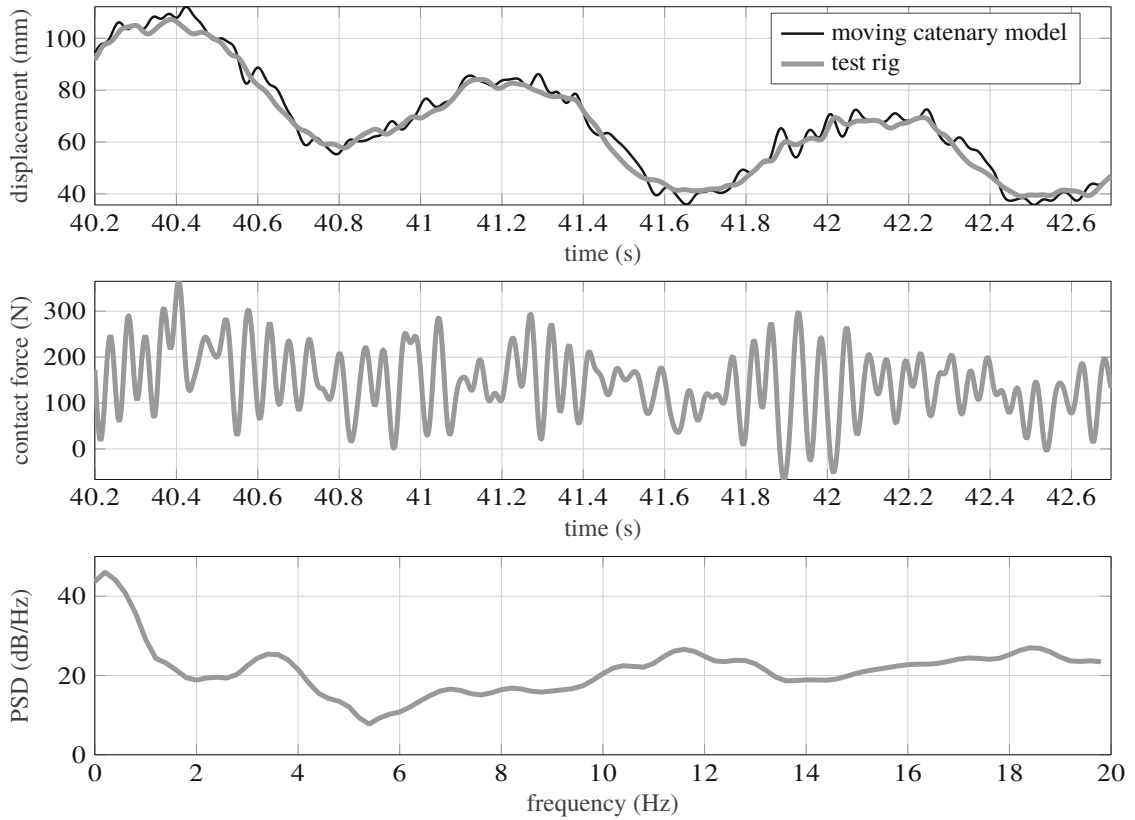


Figure 3.15 Results of a PHiL test run with a simulated 250 km/h train ride. The upper plot shows the displacement of the contact wire at the pantograph's contact point, the middle plot the resulting contact force and the lower plot shows the power spectral density of the force signal.

Chapter 4

Summary of the scientific publications

[[Publication A](#)] describes a general method to obtain highly absorbing boundary conditions of arbitrary order of finite-difference discretized wave-like PDEs. The coefficients of the boundary stencils are obtained by solving an optimization problem. Further, two performance and one stability criterion are presented and so robustness can be traded with performance by formulating a multi-objective optimization problem. The method is finally applied to two common engineering problems: the Euler-Bernoulli bending beam under axial pre-tension and the two-dimensional wave equation.

In [[Publication B](#)] a catenary model in a moving-coordinate formulation based on a physical white-box modeling process is presented that allows for great flexibility through easy parametrization. The linear time-varying finite-difference model is then used in an impedance control concept to track the catenary dynamics on a real pantograph test rig. Furthermore, consistency in the conserved quantities momentum and energy was ensured by the control concept by introducing a virtual correction force to the catenary model.

[[Publication C](#)] presents a nonlinear real-time capable finite-element model of the catenary dynamics. The model is obtained by a physical modeling process and formulated in a moving (train-fixed) coordinate system. An absorbing boundary control scheme prevents unrealistic wave reflections at artificial domain boundaries. A reduced linear version of the catenary model is used in a model predictive impedance control concept to emulate the catenary dynamics on a pantograph PHiL test rig.

[[Publication D](#)] further investigates the boundary controller presented in [[Publication C](#)]. For example the influence of different implementations of the nonlinear dispersion relation on the accuracy of the absorption is investigated.

Chapter 5

Scientific contributions of the applicant

The scientific contributions of this work are applicable to various forms of HiL test rigs and are exemplarily demonstrated on an actual pantograph test rig. The derived absorbing boundary methods are of generic nature and can be employed on different types of PDEs where the computational domain would otherwise be too large for real-time computation.

Furthermore, an efficient way of modeling the catenary dynamics was shown and a real-time capable simulation method handling the sparse system matrices while dealing with nonlinearities was developed.

On a last step, trustworthy PHiL test runs were conducted by not only accurately tracking the impedance model dynamics but also ensuring consistency in the conserved quantities energy and momentum.

Summarized, the scientific contributions of this work are:

Catenary modeling

- physical-based modeling process that allows for easy parametrization and great flexibility
- moving-coordinate formulation and incorporation of the nonlinear dropper behavior
- real-time simulation of the catenary model by an efficient implementation of a solver for nonlinear finite-element discretized dynamics

Absorbing boundaries for PDEs

- generic optimization-based approach for obtaining stencil coefficients in FD-discretized wave-like PDEs
 - derivation of two performance objectives (output-error and reflection coefficient)
 - ensuring stability via constraints or as a second objective
 - multi-objective optimization allows tuning the performance/stability trade-off
 - formulation of absorbing boundaries for the EBB under axial pre-tension

- absorbing boundaries via control
 - emulation of a perfectly matched layer by utilizing forces and torques acting on boundary nodes to realize absorption/damping profile
 - modal-based derivation of a reference trajectory
 - application to the EBB in moving coordinates

PHiL test rig control

- model predictive impedance control of nonlinear dynamics
- tracking of FD and FE discretized catenary dynamics
- consistency in the conserved quantities momentum and energy by introducing a virtual correction force
- implementation on a state-of-the-art real-time computing platform and demonstration of the developed methods by PHiL tests.

Bibliography

- [Publication A] A. Schirrer, E. Talic, G. Aschauer, M. Kozek, and S. Jakubek. “Optimization based determination of highly absorbing boundary conditions for linear finite difference schemes.” In: *Journal of Sound and Vibration* 365 (2016), pp. 45–69.
DOI: [10.1016/j.jsv.2015.12.006](https://doi.org/10.1016/j.jsv.2015.12.006).
- [Publication B] A. Schirrer, G. Aschauer, E. Talic, M. Kozek, and S. Jakubek. “Catenary Emulation for Hardware-in-the-Loop Pantograph Testing with a Model Predictive Energy-Conserving Control Algorithm.” In: *Mechatronics* 41 (2017), pp. 17–28.
DOI: [10.1016/j.mechatronics.2016.11.002](https://doi.org/10.1016/j.mechatronics.2016.11.002).
- [Publication C] G. Aschauer, A. Schirrer, M. Kozek, and S. Jakubek. “PHiL pantograph testing via FE-based catenary model with absorbing boundaries.” In: *Control Engineering Practice* 88 (2019), pp. 97–109.
DOI: [10.1016/j.conengprac.2019.04.006](https://doi.org/10.1016/j.conengprac.2019.04.006).
- [Publication D] A. Schirrer, G. Aschauer, M. Kozek, and S. Jakubek. “Power-HIL-Emulation der Dynamik einer Zug-Oberleitung mittels Echtzeit-Finite-Elemente-Modell in bewegten Koordinaten und modellprädiktiver Regelung.” In: *at – Automatisierungstechnik* 68.8 (2020), pp. 641–653.
DOI: [10.1515/auto-2020-0009](https://doi.org/10.1515/auto-2020-0009).
- [1] M. Arnold and B. Simeon. “Pantograph and catenary dynamics: A benchmark problem and its numerical solution.” In: *Applied Numerical Mathematics* 34.4 (2000), pp. 345–362.
- [2] J. Ambrosio, J. Pombo, M. Pereira, P. Antunes, and A. Mosca. “A computational procedure for the dynamic analysis of the catenary-pantograph interaction in high-speed trains.” In: *Journal of Theoretical and Applied Mechanics* 50.3 (2012).
- [3] D. Ritzberger, E. Talic, and A. Schirrer. “Efficient simulation of railway pantograph/catenary interaction using pantograph-fixed coordinates.” In: *IFAC-PapersOnLine* 48.1 (2015). 8th Vienna International Conference on Mathematical Modelling, MATHMOD 2015, pp. 61–66.
DOI: [10.1016/j.ifacol.2015.05.083](https://doi.org/10.1016/j.ifacol.2015.05.083).

- [4] G. Aschauer, A. Schirrer, and S. Jakubek. “Realtime-capable finite element model of railway catenary dynamics in moving coordinates.” In: *2016 IEEE Conference on Control Applications (CCA)*. Sept. 2016, pp. 1078–1083.
DOI: [10.1109/CCA.2016.7587950](https://doi.org/10.1109/CCA.2016.7587950).
- [5] B. Engquist and A. Majda. “Absorbing boundary conditions for numerical simulation of waves.” In: *Proceedings of the National Academy of Sciences* 74.5 (1977), pp. 1765–1766.
- [6] J.-P. Berenger et al. “A perfectly matched layer for the absorption of electromagnetic waves.” In: *Journal of computational physics* 114.2 (1994), pp. 185–200.
- [7] D. Ritzberger, A. Schirrer, and S. Jakubek. “Absorbing boundary layer control for linear one-dimensional wave propagation problems.” In: *Journal of Vibration and Control* (2016), pp. 1–13.
DOI: [10.1177/1077546316679579](https://doi.org/10.1177/1077546316679579).
- [8] S. Jakubek, E. Luchini, A. Oberhammer, and F. Pfister. “A model-based interfacing concept for accurate power hardware-in-the-loop systems.” In: *Mathematical and Computer Modelling of Dynamical Systems* 22.1 (2016), pp. 1–20.
DOI: [10.1080/13873954.2015.1069748](https://doi.org/10.1080/13873954.2015.1069748).
- [9] G. Guennebaud, B. Jacob, et al. *Eigen v3*. <http://eigen.tuxfamily.org>. 2010.
- [10] H. Ferreau, C. Kirches, A. Potschka, H. Bock, and M. Diehl. “qpOASES: A parametric active-set algorithm for quadratic programming.” In: *Mathematical Programming Computation* 6.4 (2014), pp. 327–363.
- [11] H. Ferreau, H. Bock, and M. Diehl. “An online active set strategy to overcome the limitations of explicit MPC.” In: *International Journal of Robust and Nonlinear Control* 18.8 (2008), pp. 816–830.
- [12] G. Aschauer, A. Schirrer, and M. Kozek. “Co-Simulation of Matlab and FlightGear for Identification and Control of Aircraft.” In: *8th Vienna International Conference on Mathematical Modelling MATHMOD 2015*. Vol. 48-1. 2015, pp. 67–72.
DOI: [10.1016/j.ifacol.2015.05.071](https://doi.org/10.1016/j.ifacol.2015.05.071).
- [13] A. Schirrer, G. Aschauer, and S. Jakubek. “High-Dynamic Accurate Railway Catenary Emulation by Real-Time Mechanical Impedance Control for Pantograph Testing.” In: *Simulation and Testing for Vehicle Technology*. Ed. by C. Gühmann, J. Riese, and K. von Räden. Cham: Springer International Publishing, 2016, pp. 277–295.
DOI: [10.1007/978-3-319-32345-9_20](https://doi.org/10.1007/978-3-319-32345-9_20).

- [14] A. Schirrer, G. Aschauer, and S. Jakubek. “Hardware-in-the-Loop Testing of High-Speed Pantographs Using Real-Time Catenary Emulation.” In: *Dynamics and Control of Advanced Structures and Machines*. Ed. by H. Irschik, A. Belyaev, and M. Krommer. Cham: Springer International Publishing, 2017, pp. 75–83.
DOI: [10.1007/978-3-319-43080-5_8](https://doi.org/10.1007/978-3-319-43080-5_8).
- [15] A. Schirrer, G. Aschauer, and S. Jakubek. “Comparison of real-time models for high-fidelity hardware-in-the-loop catenary emulation in a high-dynamic pantograph test rig.” In: *Procedia Engineering* 199 (2017). X International Conference on Structural Dynamics, EURO-DYN 2017, pp. 3290–3295.
DOI: [10.1016/j.proeng.2017.09.403](https://doi.org/10.1016/j.proeng.2017.09.403).
- [16] G. Aschauer, A. Schirrer, M. Kozek, and S. Jakubek. “Realtime-capable FE-based railway catenary emulation via pantograph test rig impedance control.” In: *IFAC-PapersOnLine* 50.1 (2017). 20th IFAC World Congress, pp. 8636–8641.
DOI: [10.1016/j.ifacol.2017.08.1519](https://doi.org/10.1016/j.ifacol.2017.08.1519).

Peer-reviewed journal publications

- [Publication A] A. Schirrer, E. Talic, G. Aschauer, M. Kozek, and S. Jakubek. “Optimization based determination of highly absorbing boundary conditions for linear finite difference schemes.” In: *Journal of Sound and Vibration* 365 (2016), pp. 45–69.
DOI: [10.1016/j.jsv.2015.12.006](https://doi.org/10.1016/j.jsv.2015.12.006).
- [Publication B] A. Schirrer, G. Aschauer, E. Talic, M. Kozek, and S. Jakubek. “Catenary Emulation for Hardware-in-the-Loop Pantograph Testing with a Model Predictive Energy-Conserving Control Algorithm.” In: *Mechatronics* 41 (2017), pp. 17–28.
DOI: [10.1016/j.mechatronics.2016.11.002](https://doi.org/10.1016/j.mechatronics.2016.11.002).
- [Publication C] G. Aschauer, A. Schirrer, M. Kozek, and S. Jakubek. “PHiL pantograph testing via FE-based catenary model with absorbing boundaries.” In: *Control Engineering Practice* 88 (2019), pp. 97–109.
DOI: [10.1016/j.conengprac.2019.04.006](https://doi.org/10.1016/j.conengprac.2019.04.006).
- [Publication D] A. Schirrer, G. Aschauer, M. Kozek, and S. Jakubek. “Power-HIL-Emulation der Dynamik einer Zug-Oberleitung mittels Echtzeit-Finite-Elemente-Modell in bewegten Koordinaten und modellprädiktiver Regelung.” In: *at – Automatisierungstechnik* 68.8 (2020), pp. 641–653.
DOI: [10.1515/auto-2020-0009](https://doi.org/10.1515/auto-2020-0009).

Conference papers

- [4] G. Aschauer, A. Schirrer, and S. Jakubek. “Realtime-capable finite element model of railway catenary dynamics in moving coordinates.” In: *2016 IEEE Conference on Control Applications (CCA)*. Sept. 2016, pp. 1078–1083.
DOI: [10.1109/CCA.2016.7587950](https://doi.org/10.1109/CCA.2016.7587950).
- [12] G. Aschauer, A. Schirrer, and M. Kozek. “Co-Simulation of Matlab and FlightGear for Identification and Control of Aircraft.” In: *8th Vienna International Conference on Mathematical Modelling MATHMOD 2015*. Vol. 48-1. 2015, pp. 67–72.
DOI: [10.1016/j.ifacol.2015.05.071](https://doi.org/10.1016/j.ifacol.2015.05.071).
- [13] A. Schirrer, G. Aschauer, and S. Jakubek. “High-Dynamic Accurate Railway Catenary Emulation by Real-Time Mechanical Impedance Control for Pantograph Testing.” In: *Simulation and Testing for Vehicle Technology*. Ed. by C. Gühmann, J. Riese, and K. von Rügen. Cham: Springer International Publishing, 2016, pp. 277–295.
DOI: [10.1007/978-3-319-32345-9_20](https://doi.org/10.1007/978-3-319-32345-9_20).
- [14] A. Schirrer, G. Aschauer, and S. Jakubek. “Hardware-in-the-Loop Testing of High-Speed Pantographs Using Real-Time Catenary Emulation.” In: *Dynamics and Control of Advanced Structures and Machines*. Ed. by H. Irschik, A. Belyaev, and M. Krommer. Cham: Springer International Publishing, 2017, pp. 75–83.
DOI: [10.1007/978-3-319-43080-5_8](https://doi.org/10.1007/978-3-319-43080-5_8).
- [15] A. Schirrer, G. Aschauer, and S. Jakubek. “Comparison of real-time models for high-fidelity hardware-in-the-loop catenary emulation in a high-dynamic pantograph test rig.” In: *Procedia Engineering* 199 (2017). X International Conference on Structural Dynamics, EURO-DYN 2017, pp. 3290–3295.
DOI: [10.1016/j.proeng.2017.09.403](https://doi.org/10.1016/j.proeng.2017.09.403).
- [16] G. Aschauer, A. Schirrer, M. Kozek, and S. Jakubek. “Realtime-capable FE-based railway catenary emulation via pantograph test rig impedance control.” In: *IFAC-PapersOnLine* 50.1 (2017). 20th IFAC World Congress, pp. 8636–8641.
DOI: [10.1016/j.ifacol.2017.08.1519](https://doi.org/10.1016/j.ifacol.2017.08.1519).

Book chapters

- [13] A. Schirrer, G. Aschauer, and S. Jakubek. “High-Dynamic Accurate Railway Catenary Emulation by Real-Time Mechanical Impedance Control for Pantograph Testing.” In: *Simulation and Testing for Vehicle Technology*. Ed. by C. Gühmann, J. Riese, and K. von Rüden. Cham: Springer International Publishing, 2016, pp. 277–295.
DOI: [10.1007/978-3-319-32345-9_20](https://doi.org/10.1007/978-3-319-32345-9_20).
- [14] A. Schirrer, G. Aschauer, and S. Jakubek. “Hardware-in-the-Loop Testing of High-Speed Pantographs Using Real-Time Catenary Emulation.” In: *Dynamics and Control of Advanced Structures and Machines*. Ed. by H. Irschik, A. Belyaev, and M. Krommer. Cham: Springer International Publishing, 2017, pp. 75–83.
DOI: [10.1007/978-3-319-43080-5_8](https://doi.org/10.1007/978-3-319-43080-5_8).

Part II

Publications

Main Body of the Thesis

5.1 Publication A

A. Schirrer, E. Talic, G. Aschauer, M. Kozek, and S. Jakubek. “Optimization based determination of highly absorbing boundary conditions for linear finite difference schemes.” In: *Journal of Sound and Vibration* 365 (2016), pp. 45–69.
DOI: [10.1016/j.jsv.2015.12.006](https://doi.org/10.1016/j.jsv.2015.12.006).

Applicant’s contribution

The applicant primarily worked on problem analysis, the formulation of the output-error accuracy objective and implemented the two-dimensional wave equation test problem. Additionally, he assisted in the design and implementation of the developed methods, extended the optimization problem to tune-able parameters (e.g. angle of incident of incoming waves) and also contributed in the structuring, writing and editing of the manuscript.

5.2 Publication B

A. Schirrer, G. Aschauer, E. Talic, M. Kozek, and S. Jakubek. “Catenary Emulation for Hardware-in-the-Loop Pantograph Testing with a Model Predictive Energy-Conserving Control Algorithm.” In: *Mechatronics* 41 (2017), pp. 17–28.

DOI: [10.1016/j.mechatronics.2016.11.002](https://doi.org/10.1016/j.mechatronics.2016.11.002).

Applicant’s contribution

The applicant developed large parts of the MPC code base and incorporated the linear time-varying catenary model into the control design. Additionally, he established the complete PHiL setup and conducted simulation studies as well as the PHiL tests. He also did research on the application of the virtual correction force to ensure energy and momentum consistency, extended and implemented these methods in his control design and finally also contributed in the structuring, writing and editing of the manuscript.

5.3 Publication C

G. Aschauer, A. Schirrer, M. Kozek, and S. Jakubek. “PHiL pantograph testing via FE-based catenary model with absorbing boundaries.” In: *Control Engineering Practice* 88 (2019), pp. 97–109.

DOI: [10.1016/j.conengprac.2019.04.006](https://doi.org/10.1016/j.conengprac.2019.04.006).

Applicant’s contribution

The applicant’s work included the advancement of methodology, problem analysis, development and implementation of algorithms, as well as performing simulation studies, and conducting PHiL test runs.

Specifically, the method of the controlled absorbing boundary layers was extended to be usable in the finite-element formulation and incorporated into the nonlinear FE-catenary model that was co-developed by the applicant. The PHiL emulation setup was completely done by the applicant and simulation studies as well as the PHiL tests were conducted by him. He finally also contributed in the structuring, writing and editing of the manuscript.

5.4 Publication D

A. Schirrer, G. Aschauer, M. Kozek, and S. Jakubek. “Power-HIL-Emulation der Dynamik einer Zug-Oberleitung mittels Echtzeit-Finite-Elemente-Modell in bewegten Koordinaten und modellprädiktiver Regelung.” In: *at – Automatisierungstechnik* 68.8 (2020), pp. 641–653.

DOI: [10.1515/auto-2020-0009](https://doi.org/10.1515/auto-2020-0009).

Applicant’s contribution

The applicant’s work included problem analysis, advancement of methodology, development and implementation of algorithms, as well performing simulation studies and data analysis. He also contributed in the structuring, writing and editing of the manuscript.

Curriculum Vitae

CURRICULUM VITAE

PERSONAL DETAILS

Name	Guilherme Aschauer
Date of birth	February 20, 1987
Place of birth	Porto Alegre (Brazil)
Nationality	Austria
Address	An der oberen Alten Donau 15/25 1210 Vienna Austria
Email address	aschauer@mailbox.org
Phone number	+43 650 753 68 39



EDUCATION

2014 – today	Doctoral studies in Mechanical Engineering, TU Wien (Vienna University of Technology)
2011 – 2014	Master's study in Mechanical Engineering, TU Wien
Spring 2011	Exchange semester at ETH Zürich
2007 – 2011	Bachelor's study in Mechanical Engineering, TU Wien
2006 – 2007	Studies in Computer Science, TU Wien
2001 – 2006	Higher technical college for engineering (Computer Science), 1220 Vienna
1997 – 2001	Grammar school, Wohlmutstraße, 1020 Vienna

WORK EXPERIENCE

2017 – today	Engineer, Siemens Mobility Austria GmbH Division of Bogies & Pantographs
2014 – 2017	Project assistant, TU Wien Institute of Mechanics and Mechatronics Division of Control and Process Automation
Summer 2012	2-month internship – Koç University, Istanbul, Turkey
2007 – 2012	Part time – DO & CO Airline Catering Austria GmbH
2007	Part time – Fleura Austria Blumengroßhandel GmbH
2006 – 2007	Compulsory military service
2003 – 2005	4-week internships – s IT Solutions AT Spardat GmbH
2002	4-week internship – Grabner Instruments GmbH

IT SKILLS

Programming	C, C++, Matlab
Data base	SQL
DTP, Office	L ^A T _E X, Microsoft Office
Operating Systems	Windows, Linux
CAD	CATIA, Solidworks
Others	Matlab/Simulink, dSPACE, Siemens PLCs

LANGUAGES

German	native language
English	fluent (written and spoken)

LEISURE INTERESTS

Sports	Ice and inline hockey
Reading	
Travelling	
Vienna, May 17, 2021	Guilherme Aschauer

SCIENTIFIC PUBLICATIONS

G. Aschauer, A. Schirrer, M. Kozek, S. Jakubek. PHiL pantograph testing via FE-based catenary model with absorbing boundaries. *Control Engineering Practice*, Volume 88, 2019, pages 97–109, ISSN: 0967-0661.

DOI: 10.1016/j.conengprac.2019.04.006

A. Schirrer, G. Aschauer, M. Kozek, S. Jakubek. Power-HIL-Emulation der Dynamik einer Zug-Oberleitung mittels Echtzeit-Finite-Elemente-Modell in bewegten Koordinaten und modellprädiktiver Regelung. *at - Automatisierungstechnik*, Volume 68, Number 8, 2020, pages 641–653.

DOI: 10.1515/auto-2020-0009

A. Schirrer, G. Aschauer, E. Talic, M. Kozek, S. Jakubek. Catenary emulation for hardware-in-the-loop pantograph testing with a model predictive energy-conserving control algorithm. *Mechatronics*, Volume 41, 2017, pages 17–28, ISSN: 0957-4158.

DOI: 10.1016/j.mechatronics.2016.11.002

A. Schirrer, E. Talic, G. Aschauer, M. Kozek, S. Jakubek.. Optimization based determination of highly absorbing boundary conditions for linear finite difference schemes. *Journal of Sound and Vibration*, Volume 365, 2016, pages 45–69, ISSN: 0022-460X.

DOI: 10.1016/j.jsv.2015.12.006

TALKS AND PRESENTATIONS AT INTERNATIONAL CONFERENCES & BOOK CHAPTERS

G. Aschauer, A. Schirrer, M. Kozek. Co-Simulation of Matlab and FlightGear for Identification and Control of Aircraft. *8th Vienna International Conference on Mathematical Modelling MATHMOD 2015*, February 18–20, 2015, Vienna, Austria,.

DOI: 10.1016/j.ifacol.2015.05.071

A. Schirrer, G. Aschauer, S. Jakubek. High-Dynamic Accurate Railway Catenary Emulation by Real-Time Mechanical Impedance Control for Pantograph Testing. *Simulation and Testing for Vehicle Technology*, Ed. by C. Gühmann, J. Riese, K. Rüden, Springer International Publishing, Cham, 2016, pp. 277–295.

DOI: 10.1007/978-3-319-32345-9_20

G. Aschauer, A. Schirrer, S. Jakubek. Realtime-capable finite element model of railway catenary dynamics in moving coordinates. *IEEE Conference on Control Applications (CCA)*, September 19–22, 2016, Buenos Aires, Argentina.

DOI: 10.1109/CCA.2016.7587950

A. Schirrer, G. Aschauer, S. Jakubek. Hardware-in-the-Loop Testing of High-Speed Pantographs Using Real-Time Catenary Emulation. *Dynamics and Control of Advanced Structures and Machines*, Ed. by Hans Irschik, Alexander Belyaev, and Michael Krommer, Springer International Publishing, Cham, 2017, pp. 75–83.

DOI: 10.1007/978-3-319-43080-5_8

G. Aschauer, A. Schirrer, S. Jakubek. Realtime-capable FE-based railway catenary emulation via pantograph test rig impedance control. *20th IFAC World Congress*, July 9–14, 2017, Toulouse, France.

DOI: 10.1016/j.ifacol.2017.08.1519

A. Schirrer, G. Aschauer, S. Jakubek. Comparison of real-time models for high-fidelity hardware-in-the-loop catenary emulation in a high-dynamic pantograph test rig. *X International Conference on Structural Dynamics, EURO DYN 2017*, September 10–13, 2017, Rome, Italy.

DOI: 10.1016/j.proeng.2017.09.403